Monthly Notices of the ROYAL ASTRONOMICAL SOCIETY

MNRAS **532,** 3926–3946 (2024) https://doi.org/10.1093/mnras/stae1681
Advance Access publication 2024 July 12

Fate of supernova progenitors in massive binary systems

Tomoya Kinugawa [1,2,3]★ Shunsaku Horiuchi [4,5]★ Tomoya Takiwaki [6] and Kei Kotake [7,8]

[1]*Faculty of Engineering, Shinshu University, 4-17-1, Wakasato, Nagano-shi, Nagano 380-8553, Japan*
[2]*Research Center for Aerospace System, Shinshu University, 4-17-1, Wakasato, Nagano-shi, Nagano 380-8553, Japan*
[3]*Research Center for the Early Universe, Graduate School of Science, University of Tokyo, 7-3-1 Hongo, Bunkyo-ku, Tokyo 113-0033, Japan*
[4]*Center for Neutrino Physics, Department of Physics, Virginia Tech, Blacksburg, VA 24061, USA*
[5]*Kavli IPMU (WPI), UTIAS, The University of Tokyo, Kashiwa, Chiba 277-8583, Japan*
[6]*National Astronomical Observatory of Japan, 2-21-1 Osawa, Mitaka, Tokyo 181-8588, Japan*
[7]*Research Institute of Stellar Explosive Phenomena, Fukuoka University, 8-19-1 Nanakuma, Jonan-ku, Fukuoka-shi, Fukuoka 814-0180, Japan*
[8]*Department of Applied Physics, Faculty of Science, Fukuoka University, 8-19-1 Nanakuma, Jonan-ku, Fukuoka-shi, Fukuoka 814-0180, Japan*

Accepted 2024 July 8. Received 2024 July 6; in original form 2023 November 25

ABSTRACT

How massive stars end their lives depends on the core mass, core angular momentum, and hydrogen envelopes at death. However, these key physical facets of stellar evolution can be severely affected by binary interactions. In turn, the effectiveness of binary interactions itself varies greatly depending on the initial conditions of the binaries, making the situation much more complex. We investigate systematically how binary interactions influence core–collapse progenitors and their fates. Binary evolution simulations are performed to survey the parameter space of supernova progenitors in solar metallicity binary systems and to delineate major evolutionary paths. We first study fixed binary mass ratios ($q = M_2/M_1 = 0.5$, 0.7, and 0.9) to elucidate the impacts of initial mass and initial separation on the outcomes, treating separately Type Ibc supernova, Type II supernova, accretion-induced collapse (AIC), rapidly rotating supernova (Ibc-R), black hole formation, and long gamma ray burst (long GRB). We then conduct 12 binary population synthesis model calculations, varying the initial condition distributions and binary evolution parameters, to estimate various supernova fractions. We obtain a Milky Way supernova rate $R_{\rm SN} = (1.78–2.47) \times 10^{-2}\,{\rm yr}^{-1}$ which is consistent with observations. We find the rates of AIC, Ibc-R, and long GRB to be $\sim 1/100$ the rate of regular supernovae. Our estimated long GRB rates are higher than the observed long GRB rate and close to the low luminosity GRB rate, although care must be taken considering our models are computed with solar metallicity. Furthering binary modelling and improving the inputs one by one will enable more detailed studies of these and other transients associated with massive stars.

Key words: binaries: general – stars: black holes – gamma-ray burst: general – stars: neutron – supernovae: general.

1 INTRODUCTION

Stellar evolution holds paramount importance in astrophysics, providing a foundational framework for not only comprehending the behaviours of stars but also their profound influence on shaping the Universe. By studying how stars form, evolve, and eventually die, one can gain insights into a wide range of astrophysical phenomena, from the properties of individual stars to the formation and evolution of galaxies (Conroy 2013; Nomoto, Kobayashi & Tominaga 2013; Smith 2014; Eldridge & Stanway 2022). In particular, supernovae (SNe) and long gamma-ray bursts (long GRBs) are among the most powerful and intriguing transient phenomenon in the Universe, which are the explosions triggered by the death of massive stars (Woosley, Heger & Weaver 2002; Woosley & Bloom 2006; Gehrels, Ramirez-Ruiz & Fox 2009; Smartt 2009).

In a seminal work on stellar evolution, Heger et al. (2003) illustrated that a star's mass and metallicity determine its eventual fate (see also Woosley, Langer & Weaver 1995; Woosley et al. 2002; Woosley & Heger 2007; Sukhbold et al. 2016, for systematic studties). A variety of models are provided and they are often used in SN modelling (Umeda & Nomoto 2008; Umeda, Yoshida & Takahashi 2012; Sukhbold, Woosley & Heger 2018; Chieffi & Limongi 2020). With the ever-increasing power of supercomputers, studies of the systematic effects of the progenitor mass and metallicity have been explored in multidimensional numerical simulations of massive star collapse (Nakamura et al. 2015; Summa et al. 2016; Burrows et al. 2020; Vartanyan & Burrows 2023). Among the many insights they have provided, of particular importance is that the anisotropy of the Si/O shell is enough to alter the course of dynamical evolution of the core–collapse SN (Bollig et al. 2021). Thus, 3D simulations have been performed with limited time-scale of the Si/O burning phase to explore more realistic profiles of the progenitors (Couch et al. 2015; Müller et al. 2016b; Mocák et al. 2018; Yoshida et al. 2019; Yadav et al. 2020; Yoshida et al. 2021b).

One commonly missing ingredient in previous studies of SN progenitors is rotation. This is despite the fact that massive stars initially have high angular momentum (Wolff et al. 2006; Huang,

★ E-mail: kinugawa@shinshu-u.ac.jp (TK); horiuchi@vt.edu (SH)

Gies & McSwain 2010) and rotation affects the evolution of stars as strongly as mass and metallicity (e.g. Maeder 2009); for example, centrifugal force, angular momentum transport, and rotation-induced mixing change the stellar structure (see Langer 2012, and the refereces therein). Several evolutionary models have incorporated the impact of rotation (Heger, Langer & Woosley 2000; Heger, Woosley & Spruit 2005; Ekström et al. 2012; Georgy et al. 2012). Yoon, Langer & Norman (2006) have helped us to delineate the fate of the massive stars in the parameter space of mass, metallicity, and rotation. At the extreme, a star can completely change its evolution when it undergoes chemically homogeneous evolution (CHE) due to efficient mixing induced by rotation (Woosley & Heger 2006; Yoon et al. 2006; Aguilera-Dena et al. 2018). Although CHE may not be common, more generally stars are deformed by rotation; axisymmetric equilibrium structures of rotating stars in two spatial dimensions have been obtained (see Ogata et al. 2023, and the refereces therein). It is imperative to also acknowledge the intricate connection of magnetic fields and rotation in stellar evolution (see Keszthelyi 2023, and refereces therein). A way to handle the shape of the magnetic fields was recently developed (Takahashi & Langer 2021). The effect of rotation and magnetic fields are eagerly studied by 3D simulations in the phases right before the core collapse (Varma & Müller 2021; Yoshida et al. 2021a; Fields 2022; McNeill & Müller 2022). The strength of the magnetic field and rotation of stellar cores are thought to even dictate the outcome of explosion, including explosion energies and morphologies, as well as occurrence of SNe versus long GRBs (e.g. Iwakami, Nagakura & Yamada 2014; Summa et al. 2018; Kuroda et al. 2020; Takiwaki, Kotake & Foglizzo 2021; Matsumoto et al. 2022; Obergaulinger & Aloy 2022; Bugli et al. 2023; Hsieh et al. 2024; Shibagaki et al. 2024; Varma, Müller & Schneider 2023).

Therefore, it is not surprising that binary interactions have garnered substantial attention due to their impact on stellar rotation, involving factors such as tidal interactions in binary systems and mass transfer. Moreover, observational evidence suggests a high binary formation rate among high-mass stars (Kobulnicky & Fryer 2007; Mason et al. 2009; Chini et al. 2012; Sana et al. 2012, 2013; Kobulnicky et al. 2014; Moe & Di Stefano 2017). Efforts to incorporate binary effects into stellar evolution codes are ongoing (Cantiello et al. 2007; Patton & Sukhbold 2020; Laplace et al. 2021; Schneider, Podsiadlowski & Müller 2021), including even to SN modelling (Vartanyan et al. 2021). The most famous example of a SN from a binary system is perhaps SN1987A (e.g. Menon & Heger 2017; Urushibata et al. 2018; Ono et al. 2020; Utrobin et al. 2021; Nakamura, Takiwaki & Kotake 2022). Observations of the explosion site are still ongoing (Cigan et al. 2019; Larsson et al. 2023). As another example, the SN that created Cassiopeia A may also have been a binary system (Hirai et al. 2020). Also, Betelgeuse may experience a stellar merger (Chatzopoulos et al. 2020). To make a double neutron star system, an ultra-stripped SN is considered necessary, motivating again binary evolution (Tauris et al. 2017; Yoshida et al. 2017; Müller et al. 2018; Hijikawa et al. 2019). The relative rates of different types of SNe (De Donder & Vanbeveren 1998; Eldridge, Izzard & Tout 2008; Briel et al. 2022), the SN progenitor studies (Eldridge et al. 2013; Eldridge & Maund 2016), runaway star evolutions as progenitors of SNe and long GRBs (Eldridge, Langer & Tout 2011), the rate of SN from progenitors with enhanced rotation (Popov & Prokhorov 2006; Bogomazov & Popov 2009) and metallicity dependence and cosmic evolution of SN rates (De Donder & Vanbeveren 2003; Briel et al. 2022) are calculated by binary evolution calculations. The rate and progenitors of long GRBs are also calculated by binary evolution study (Belczynski et al. 2007; Kinugawa & Asano 2017; Kinugawa, Harikane & Asano 2019; Chrimes, Stanway & Eldridge 2020).

Nevertheless, while previous studies have explored the contribution of binaries to SNe in specific cases, a systematic understanding akin to the well-established scenario of single stars, as outlined by Heger et al. (2003) and Yoon et al. (2006), remains lacking. To bridge this gap, population synthesis methods emerge as indispensable tools, enabling systematic exploration under a range of assumptions regarding stellar and binary physics, in particular wind mass-loss, mass transfer, and common envelope treatments (Belczynski, Kalogera & Bulik 2002; Hurley, Tout & Pols 2002; Kinugawa et al. 2014; De Marco & Izzard 2017; Zapartas et al. 2017; Stanway & Eldridge 2018; Spera et al. 2019; Breivik et al. 2020; Tanikawa et al. 2020; Riley et al. 2022; Fragos et al. 2023). The population synthesis method is a numerical calculation technique widely used in binary studies. It is employed to study the evolution and statistical properties of binary stellar systems considering various physics of binary interactions. For example, population synthesis can estimate the gravitational wave sources from compact binary mergers (e.g. Belczynski et al. 2002; Dominik et al. 2013; Kinugawa, Nakamura & Nakano 2020, 2021a,b,c) and have predicted the massive stellar-mass binary black hole mergers (Kinugawa et al. 2014, 2016). The impact of the binary evolution on the Diffuse SN Neutrino Background (DSNB) have been studied (Horiuchi et al. 2021). In such studies, the distribution of He or CO core mass is important (Patton, Sukhbold & Eldridge 2022; Fragos et al. 2023).

It is in these contexts that we investigate systematically how binary interactions influence SN progenitors. Using simplified models, we focus in particular on the final fates of massive stars: either a 'standard' Type II SN, a stripped Ibc SN, a rapidly rotating SN, an accretion induced collapse (AIC), a collapse to black hole, or a long GRB. This paper is organized as follows. In Section 2, we describe how to calculate the binary interactions, the stellar evolution, and how to determine the SNe type. Section 3 shows our parameter survey and the binary population synthesis calculations for SNe. In Section 4, we describe the summary of this paper and discussion comparison with previous studies and uncertainties.

2 METHODS

We use the binary population synthesis code in Kinugawa et al. (2014) which is updated from the BSE code (Hurley, Pols & Tout 2000; Hurley et al. 2002) in order to calculate binary evolution effects for SNe. In this section, we describe the main binary effects which change stellar masses and the calculation methods. The other binary interactions are described in Appendix A.

2.1 Stability of mass transfer

If the Roche lobe around a star is fulfilled, the material of the stellar surface is transferred to its companion through the L1 point. The Roche lobe radius of the donor star is approximately described as (Eggleton 1983)

$$R_{\rm L,1} \simeq \frac{0.49 q_1^{2/3}}{0.6 q_1^{2/3} + \ln(1+q_1^{1/3})} a \,, \tag{1}$$

where a, $q_1 = M_1/M_2$, M_1, and M_2 are the orbital separation, the mass ratio, the mass of the donor, and the mass of the accretor, respectively.

When the mass transfer is dynamically unstable, i.e. the orbit shrink too rapidly that the accretor star will plunge into the envelope

of the donor star, the mass transfer become a common envelope phase. On the other hand, when the mass transfer is dynamically stable, the mass transfer continue stably. This case is called the Roche lobe overflow. The dynamical stability of mass transfer is determined by how the stellar radius of the donor star is changed by the mass-loss and by how the Roche lobe radius is changed by the mass transfer.

In order to consider the dynamical stability of the mass transfer, we use $\zeta_{\rm L} = {\rm dlog}R_{\rm L,1}/{\rm dlog}M_1$, and $\zeta_{\rm ad} = ({\rm dlog}R_1/{\rm dlog}M_1)_{\rm ad}$. Here, $\zeta_{\rm L}$ is the response of the Roche lobe radius $R_{\rm L,1}$ to the change in the mass of the donor star M_1 and $\zeta_{\rm ad}$ is the response of the radius of the donor star R_1 to changes in the mass of the donor star within the dynamical time-scale. When $\zeta_{\rm L} > \zeta_{\rm ad}$, the Roche lobe radius will be much smaller than the stellar radius by the mass transfer in the dynamical time-scale. In this case, the mass transfer becomes a common envelope. On the other hand, when $\zeta_{\rm L} > \zeta_{\rm ad}$, the donor stellar radius will be much smaller than the Roche lobe radius by the mass transfer in the dynamical time-scale. In this case, the mass transfer is treated as the Roche lobe overflow. $\zeta_{\rm L}$ is a function of the mass ratio and the separation of the binary, described as (Eggleton 1983, 2011)

$$\zeta_{\rm L} = \frac{{\rm dlog}R_{\rm L,1}}{{\rm dlog}M_1} \tag{2}$$

$$= \frac{(0.33 + 0.13q_1)(1+\beta q_1) + 2\beta(q_1^2 - 1) - (1-\beta)q_1}{1+q_1}. \tag{3}$$

where β is the accretion parameter of the mass transfer. On the other hand, $\zeta_{\rm ad}$ strongly depends on the evolutionary stage of the donor star. When the donor star is in the red giant phase, $\zeta_{\rm ad}$ is described as

$$\zeta_{\rm ad} = -1 + \frac{2}{3}\frac{M_1}{M_{\rm env,1}}. \tag{4}$$

When the donor star is in other evolutionary phases, $\zeta_{\rm ad}$ is 2.59, 6.85, 1.95, and 5.79 for the main sequence phase, the Hertzsprung gap phase (Hjellming 1989), the naked-He main sequence phase and the naked-He giant star (Ivanova et al. 2003; Belczynski et al. 2008), respectively.

2.2 Roche lobe overflow

When the star starts mass transfer ($R_1 > R_{\rm L,1}$) and the mass transfer is dynamically stable ($\zeta_{\rm ad} > \zeta_{\rm L}$), the Roche lobe overflow occurs. In order to calculate the mass transfer rate, we use the fitting formula by Hurley et al. (2002),

$$\dot{M}_1 = F(M_1)\left[\ln\left(\frac{R_1}{R_{\rm L,1}}\right)\right]^3 \ {\rm M}_\odot \ {\rm yr}^{-1}, \tag{5}$$

where

$$F(M_1) = 3\times10^{-6}\left\{\min\left[\left(10\frac{M_1}{10\ {\rm M}_\odot}\right), 5.0\right]\right\}^2. \tag{6}$$

As the radius of the donor changes by the Kelvin–Helmholtz (KH) time-scale, the maximum value of the mass transfer rate from the donor is given by

$$\dot{M}_{1,\rm max} = \frac{M_1}{\tau_{\rm KH,1}}, \tag{7}$$

where $\tau_{\rm KH,1}$ is the KH time-scale of the donor.

The accretion rate to the accretor is described as

$$\dot{M}_2 = -\beta\dot{M}_1. \tag{8}$$

However, if the accretor is a white dwarf, a neutron star, or a black hole, we consider the mass accretion rate is limited by the Eddington accretion rate described by

$$\dot{M}_{\rm Edd} = -\frac{4\pi c R_2}{\kappa_{\rm T}} = 2.08\times10^{-3}(1+X)^{-1}\left(\frac{R_2}{\rm R_\odot}\right) \ {\rm M}_\odot \ {\rm yr}^{-1}, \tag{9}$$

where R_2, $\kappa_{\rm T} = 0.2(1+X)$ cm^2 g^{-1}, and $X = 0.76$ are the stellar radius of the accretor, the Thomson scattering opacity, and the hydrogen mass fraction, respectively.

We calculate the spin angular momentum evolution of stars in a binary system during the RLOF. The spin angular momentum is carried from the donor to the accretor. We estimate the spin angular momentum loss of the donor in this process with a thin shell approximation:

$$\frac{{\rm d}J_{\rm sp,1}}{{\rm d}t} = \frac{2}{3}\dot{M}_1 R_1^2 \Omega_{\rm spin,1}, \tag{10}$$

where $\Omega_{\rm spin,1}$ is the spin angular velocity of the donor. For the spin angular momentum of the accretor, we consider whether the transferred mass accretes via an accretion disc or not. First, if there is no accretion disc, i.e. the secondary radius is larger than the critical radius described by

$$r_{\rm cri} = 0.07225a(q_2(1+q_2))^{1/4}, \tag{11}$$

where $q_2 = M_2/M_1$ (Lubow & Shu 1975; Ulrich & Burger 1976; Hurley et al. 2002), we assume that the angular momentum of the transferred mass evaluated by using the critical radius is added directly to the spin angular momentum of the accretor. Thus, the spin angular momentum transferred to the accretor is calculated as

$$\frac{{\rm d}J_{\rm sp,2}}{{\rm d}t} = \dot{M}_2\sqrt{GM_2 r_{\rm cri}}. \tag{12}$$

Alternatively, if the transferred mass accretes through a disc, the spin angular momentum of the accretor increases assuming that the transferred mass falls onto the stellar surface of the accretor with the Keplerian velocity. Then the spin angular momentum transferred via the accretion disc is estimated as

$$\frac{{\rm d}J_{\rm sp,2}}{{\rm d}t} = \dot{M}_2\sqrt{GM_2 R_2}. \tag{13}$$

2.3 Common envelope

If the companion star plunges into the primary star which has a core and envelope structure due to an eccentric orbit, or mass transfer becomes dynamically unstable ($\zeta_{\rm L} > \zeta_{\rm ad}$), the binary becomes a common envelope phase. In this paper, we use the $\alpha\lambda$ formalism for calculating the common envelope phase evolution (Webbink 1984), and the orbital separation just after the common envelope phase $a_{\rm f}$ is calculated by the following energy budget if the accretor star is not a giant star,

$$\alpha\left(\frac{GM_{\rm c,1}M_2}{2a_{\rm f}} - \frac{GM_1M_2}{2a_{\rm i}}\right) = \frac{GM_1M_{\rm env,1}}{\lambda R_1}. \tag{14}$$

Here, $M_{\rm c,1}$ and $M_{\rm env,1}$ are the core and envelope mass of the donor star, M_2 is the mass of the accretor star, and $a_{\rm i}$ is the separation just before the common envelope phase. The common envelope parameters are α and λ, where α is the parameter of the efficiency showing how much orbital energy is used to strip the stellar envelope, and λ is the parameter of the binding energy of the envelope.

When the accretor star is also a giant star, the orbital energy is used not only to strip the envelope of the donor star, but also to strip the envelope of the accretor star. In this case, the orbital separation

just after the common envelope phase $a_{\rm f}$ is calculated as

$$\alpha\left(\frac{GM_{1\rm c}M_{2\rm c}}{2a_{\rm f}}-\frac{GM_1M_2}{2a_{\rm i}}\right)=\frac{GM_1M_{1\rm env}}{\lambda R_1}+\frac{GM_2M_{2\rm env}}{\lambda R_2}, \quad (15)$$

where $M_{2\rm c}$, $M_{2\rm env}$, and R_2 are the core and envelope mass and radius of accretor star.

2.4 Merged remnant and rotation effect

When the common envelope phase occurs, we estimate the separation just after the common envelope phase $a_{\rm f}$, and check whether the binary has coalesced within the common envelope phase or not. When $a_{\rm f}$ is smaller than the sum of the remnant stellar radii, the binary has merged. Additionally, when the post-MS star does not reach the Hayashi track nor ignite helium burning, such a star, the so-called a Hertzsprung gap star, might not have a clear core-envelope structure. In this case, we also assume the binary merges (Taam & Sandquist 2000; Belczynski et al. 2008). If a binary merges before CCSNe, we treat the merged product as rapidly rotating with Kepler velocity.

Rapid rotation can enhance the material mixing inside the star. Horiuchi et al. (2021) showed the percentage increase of the carbon-oxygen (CO) core mass of pre-CCSN with respect to the non-rotating case, based on Takahashi, Umeda & Yoshida (2014) and Limongi (2017). For massive stars with the zero-age main sequence mass $M_{\rm ZAMS} > 13\,M_\odot$, we consider the enhancing fraction of the CO core mass with respect to the non-rotating counterpart having the same total mass as

$$f_L = 53.4M_{\rm ZAMS}^{-3/2}+0.847, \quad (16)$$

from Limongi's models (Limongi 2017). For $M_{\rm ZAMS} < 13\,M_\odot$,

$$f_T = 0.123M_{\rm ZAMS}+0.392, \quad (17)$$

from Takahashi model (Horiuchi et al. 2021). Note that in all cases, if the CO core mass estimated by the above formulae exceeds the total stellar mass, we limit the CO core mass to the total stellar mass.

Just after the merger, the merged remnant has a high angular momentum, from the orbital angular momentum. We assume the angular momentum of merged remnant $J_{\rm merge}$ as the Kepler angular momentum. On the other hand, since the merged remnant loses angular momentum by the stellar wind mass-loss, we consider the angular momentum mass-loss described by

$$\Delta J = \frac{2}{3}\Delta M R^2\Omega_{\rm spin} = \frac{2}{3k}\frac{\Delta M}{M}J, \quad (18)$$

where ΔM is the stellar wind mass-loss, M, R, $\Omega_{\rm spin}$, k, and J are the mass, radius, spin angular velocity, moment of inertia factor, and angular momentum of the merged remnant, respectively. We assume $k = 0.15$ which is the value of the red giant branch. The angular momentum of the merged remnant just before the SN is described as

$$J_{\rm preSN} = J_{\rm merge}\left(\frac{M_{\rm preSN}}{M_{\rm merge}}\right)^{\frac{2}{3k}}, \quad (19)$$

where $M_{\rm preSN}$ and $M_{\rm merge}$ are the total stellar mass of the merged remnant just before SN and the mass of the merged remnant just after the merger. We calculate the angular momentum of the CO core of the merged remnants just before SN as

$$J_{\rm CO} = \frac{M_{\rm CO}R_{\rm CO}^2}{M_{\rm preSN}R_{\rm preSN}^2}J_{\rm preSN}, \quad (20)$$

Table 1. SN types considered in this work.

SN type	CO core mass	a/M	Envelope type
AIC	$M_{\rm CO} < 1.34\,{\rm M}_\odot$	–	ONe WD
II	$1.34\,{\rm M}_\odot < M_{\rm CO} < 5\,{\rm M}_\odot$	–	yes H
Ibc	$1.34\,{\rm M}_\odot < M_{\rm CO} < 5\,{\rm M}_\odot$	< 1	no H
Ibc-R	$1.34\,{\rm M}_\odot < M_{\rm CO} < 5\,{\rm M}_\odot$	> 1	no H
BH	$5\,{\rm M}_\odot < M_{\rm CO}$	< 1	either
long GRB	$5\,{\rm M}_\odot < M_{\rm CO}$	> 1	no H

where $M_{\rm CO}$ and $R_{\rm CO}$ are the mass and the radius of the CO core, and $R_{\rm preSN}$ is the radius of the star just before SN. We estimate $R_{\rm CO}$ using the fitting formula,

$$R_{\rm CO} = \frac{1.23\times10^{-3}+8.06\times10^{-2}M_{\rm CO}-3.31\times10^{-3}M_{\rm CO}^2}{1+0.467M_{\rm CO}-3.03\times10^{-2}M_{\rm CO}^2}{\rm R}_\odot, \quad (21)$$

based on the mass–radius relation from Giacobbo, Mapelli & Spera (2017).

2.5 Determination of SN type

To study the SN explosions, we categorize the SN into six types, based on the progenitor CO core mass ($M_{\rm CO}$), angular momentum ($a_{\rm CO}/M_{\rm CO} = cJ_{\rm CO}/GM_{\rm CO}^2$), and the presence of a Hydrogen envelope (see Table 1), extending the treatment in Yoon et al. (2006).

First, since our binary evolution code stops at C ignition, we consider the CO core mass criterion for SNe of $1.34{\rm M}_\odot$ at C ignition. Although the value of the Chandrasekhar mass is $1.37{\rm M}_\odot$, the progenitor can increase its CO core mass by helium shell burning (Hijikawa et al. 2019). If the CO core mass is between $1.34\,{\rm M}_\odot$ and $5\,{\rm M}_\odot$, and the progenitor retains its hydrogen envelope, we classify them as Type II SNe, regardless of the angular momentum. Other groups have used the criterion of minimum hydrogen envelope mass $0.003{\rm M}_\odot$ (e.g. Eldridge et al. 2013) or $0.001{\rm M}_\odot$ (e.g Eldridge et al. 2008), but we use the criterion as exactly no hydrogen for simplicity. Second and third involve the same CO core mass range but progenitors that have lost their hydrogen envelopes. If the angular momentum is less than 1 ($a_{\rm CO}/M_{\rm CO} < 1$) we classify them as Type Ibc SNs, while if the angular momentum is greater than 1 ($a_{\rm CO}/M_{\rm CO} > 1$) we classify them as rapidly rotating SNe (Ibc-R), which might link to broad-lined Type Ic SNe. We expect the formation of rapidly rotating neutron stars, which may show different explosions from the normal SNe (MHD-driven explosion, see e.g. Obergaulinger, Janka & Aloy 2014 or explosions driven by low-T/W instability, see, e.g. Takiwaki et al. 2021). Fourth involves CO core masses less than $1.34M_\odot$. If such progenitors is Oxygen-Neon white dwarf (ONe WD) and undergo explosions due to accretion, they are designated as accretion-induced collapse (AIC) SNe. Fifth and sixth concern progenitors with CO core masses greater than $5\,{\rm M}_\odot$. If $a_{\rm CO}/M_{\rm CO} < 1$, they are classified as black hole formation events. We do not classify further by the presence or not of a Hydrogen envelope, due to the explosion likely appearing more similar to shock breakout than supernovae (Lovegrove, Woosley & Zhang 2017). On the other hand, if $a_{\rm CO}/M_{\rm CO} > 1$ and there are no Hydrogen envelope, they are identified as long GRBs. We assume that if the star with high angular momentum has a Hydrogen envelope, it loses the angular momentum due to efficient mass-loss, and it cannot explode as long GRB or Ibc-R.

We should keep in mind the limitation of such a simple classification. Patton et al. (2022) employ more complex criteria (Fryer

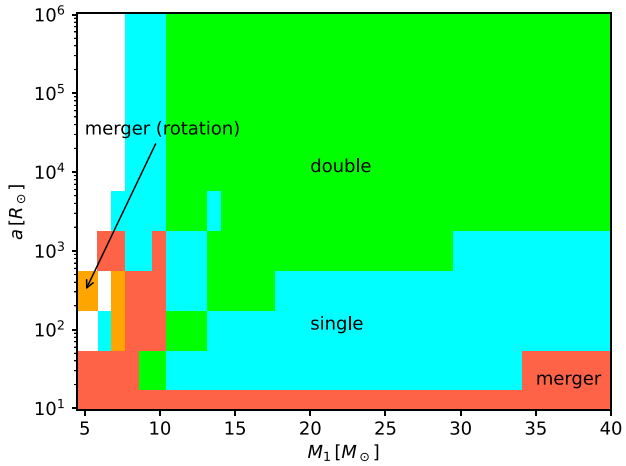

Figure 1. The binary progenitors of SNe in the mass ratio $q = 0.7$ case. Here, 'double' and 'single' refer to binary systems where both stars are core–collapse progenitors and where only one of the stars are core–collapse progenitors, respectively. Binary systems where the stars merge before core collapse are labelled 'merger'. Systems that merge and create a light mass star that only core collapse after considering rotation effects are labelled 'merger (rotation)'. See the text for details.

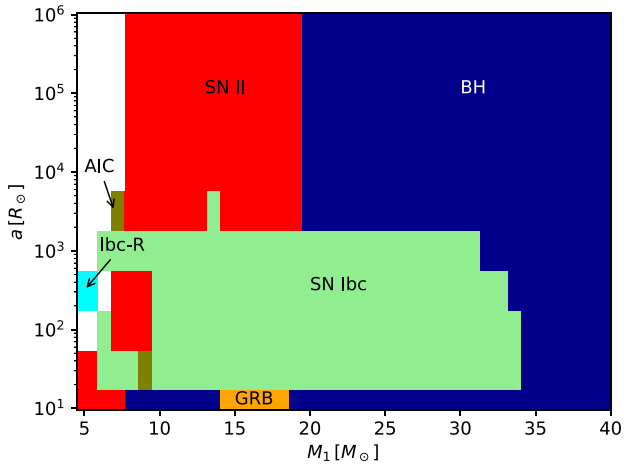

Figure 2. SN type of primary star in the $q = 0.7$ case. See Table 1 for SN type classifications.

et al. 2012; Ertl et al. 2016) and the results are shown in their fig. 4. Though the bifurcation of NS and BH is not the sole function of $M_{\rm CO}$, we still see some general trend that BH appears where $M_{\rm CO} > 5\,{\rm M}_\odot$. Schneider et al. (2021) employ the criteria of Müller et al. (2016a). In their fig. 7, BH appears in $7\,{\rm M}_\odot < M_{\rm CO} < 8\,{\rm M}_\odot$ and $14\,{\rm M}_\odot < M_{\rm CO}$. Burrows et al. (2020) and other studies claim that black holes tend to appear in a mass range of $13\,{\rm M}_\odot < M_{\rm ZAMS} < 15\,{\rm M}_\odot$, which correspond to $2\,{\rm M}_\odot < M_{\rm CO} < 3\,{\rm M}_\odot$. Such new scenarios should be tested in the future.

It is hard to estimate the angular momentum of the final compact object, WD, NS, or BH from the angular momentum of the CO core. This study treats the angular momentum in a qualitative way. Here, we introduce a simple treatment in the previous studies for further improvement. The angular momentum of CO core can be distributed to the central objects and accretion discs. See section 8.3.4 in Fragos et al. (2023) for this issue. Numerical simulations would be also useful to map the angular momentum from the core to the compact object (Sekiguchi & Shibata 2011; Fujibayashi et al. 2023).

3 MODELS AND CALCULATION RESULTS

3.1 Parameter survey

We first conduct a parameter survey of solar metal binary evolution, by performing binary evolution calculations with fixed mass ratios, $q = M_2/M_1$, and binary parameters in circular orbits. We explore the impacts of initial mass and initial separation on binary evolution and how it influences SN outcomes. We calculate three fixed mass ratio models, $q = 0.5$, 0.7, and 0.9. In each model, we calculate the initial mass from $3\,{\rm M}_\odot$ to $100\,{\rm M}_\odot$ and the initial separation $a_{\rm ini}$ from $10\,{\rm R}_\odot$ to $10^6\,{\rm R}_\odot$. The initial eccentricity is set to zero. We assume $\beta = 1$, $\alpha\lambda = 1$, and no pulsar kick.

In this section, we focus on the $q = 0.7$ model, and describe the $q = 0.5$ and $q = 0.9$ models in Appendix B. Fig. 1 shows the progenitor of the SN. If SN progenitors do not merge before the core collapse, we split these into binary systems where both stars are core–collapse progenitors (double) and binary systems where only one of the stars are core–collapse progenitors (single). If the binary stars merge before core collapse, we split these into binary systems where the progenitors become core–collapse progenitors as a result of rotational effects (merger rotation), and binary systems where the progenitor become core–collapse progenitors independently of rotational effects (merger) (see Horiuchi et al. 2021, for similar classification).

Binary calculations with $a = 10^6\,{\rm R}_\odot$ are effectively single stellar evolutions. However, when the initial separation is less than $\sim 10^4\,{\rm R}_\odot$, the SN progenitors can interact with the companion star and qualitatively change the SN progenitors. Fig. 1 shows that the influence of binary interactions depends strongly on the evolution separation. In the range $a \simeq 10^{1.5}\,{\rm R}_\odot$ to $a \simeq 10^3\,{\rm R}_\odot$, a massive binary where both stars are originally expected to undergo SNe becomes a single core–collapse system due to binary interactions. After the primary star become a SN or a core collapse, the secondary star reaches the Hertzsprung gap and makes a common envelope with the primary compact object. At that time, the secondary star disappears due to merging with the primary compact object during the common envelope phase. In the range $a \lesssim 10^{1.5}\,{\rm R}_\odot$, a massive binary will merge due to binary interactions before a SN. In particular, even if the primary star starts with a mass lower than the criterion for SN explosion, the binary interaction can enable it to become a SN. We see this new channel appear for close binaries $a \lesssim 10^3\,{\rm R}_\odot$. The effect of rotation amplifies this effect by increasing the core mass by mixing (Horiuchi et al. 2021).

In Figs 2 and 3, we show the fates of the primary star and the secondary star, respectively, as functions of the ZAMS mass and binary separation. For the secondary, white regions with close separation represent cases where mass is lost in the common envelope phase and the secondary star does not experience core collapse. If the SN progenitor is effectively a single star ($a_{\rm ini} \gtrsim 10^4\,{\rm R}_\odot$), they evolve only to Type II SN or BH, depending on the CO core mass. Figs 4 and 5 show the CO core mass as functions of the ZAMS mass and binary separation, illustrating this dependence. In the high separation regime, the CO core mass is determined solely by the initial mass, with a larger initial mass leading to a larger CO core mass. When M_1 or M_2 becomes larger than $\sim 20\,{\rm M}_\odot$, $M_{\rm CO}$ becomes $\geq 5\,{\rm M}_\odot$ and BH is formed in our classification. The angular momentum of the CO core is negligible in the case of effectively single stellar evolution, because the majority of the angular momentum is held by

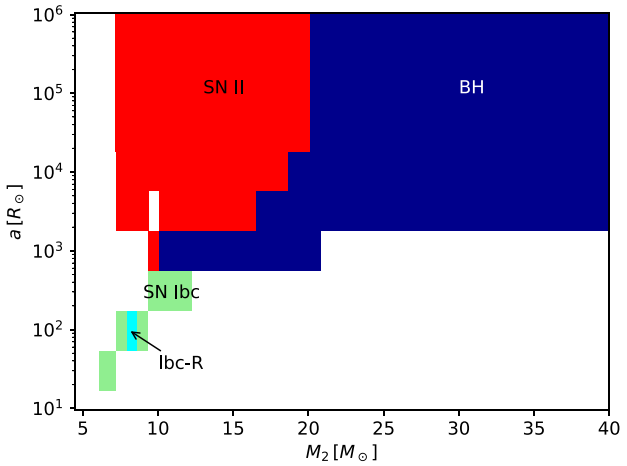

Figure 3. SN type of secondary star in the $q = 0.7$ case. Note that the results of merged stars are omitted here and shown instead in Fig. 2. The parameter region shown is thus limited to the double system labelled in Fig. 1.

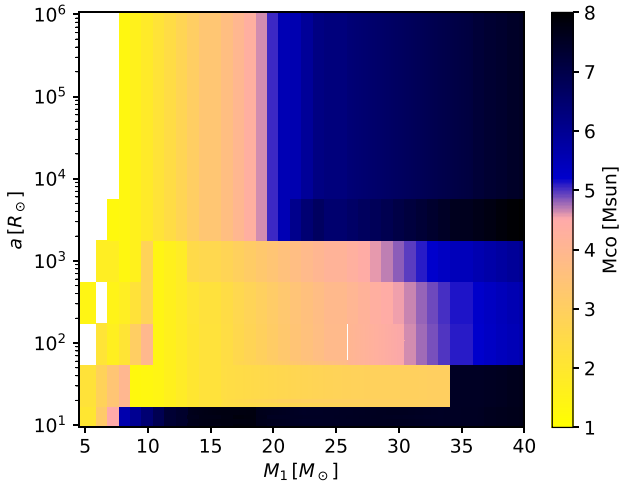

Figure 4. CO core mass of primary star in the $q = 0.7$ case.

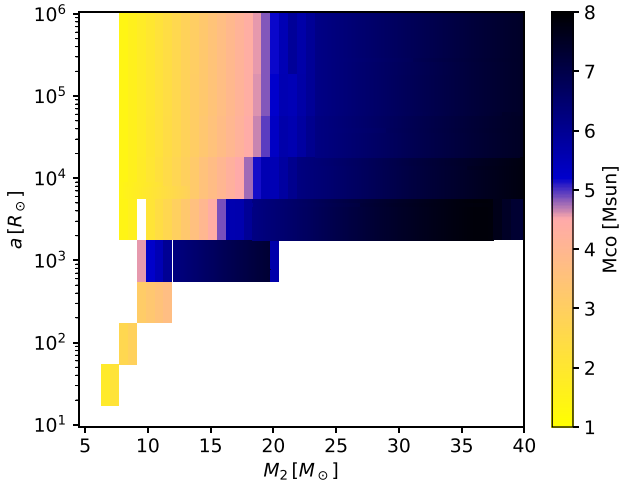

Figure 5. CO core mass of secondary star in the $q = 0.7$ case.

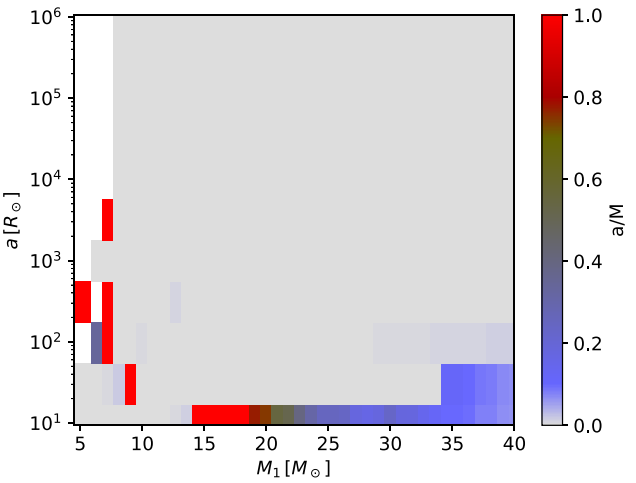

Figure 6. Angular momentum of primary star in the $q = 0.7$ case.

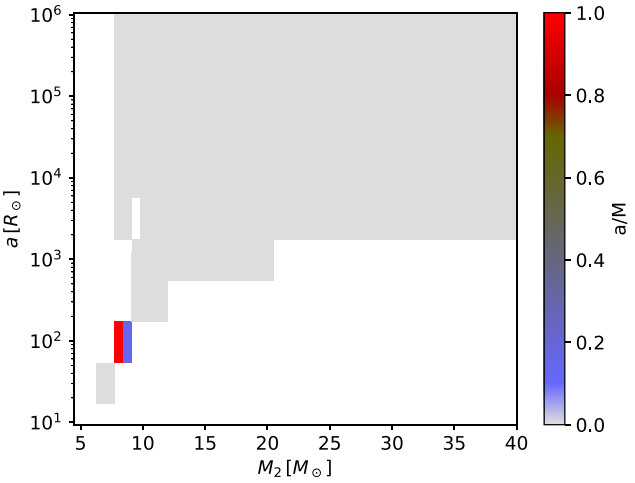

Figure 7. Angular momentum of secondary star in the $q = 0.7$ case.

the hydrogen envelope, and there is angular momentum loss due to stellar wind mass loss. We can confirm this in Figs 6 and 7, where we show the angular momentum as functions of the ZAMS mass and binary separation.

Fragos et al. (2023) shows similar results. In their fig. 4, $M_{\rm CO}$ is shown as a function of $M_{\rm ZAMS}$. In the range of $M_{\rm ZAMS} < 40\,{\rm M}_\odot$, $M_{\rm CO}$ almost linearly increases and is consistent with our results. In their fig. 30, BH appear $20\,{\rm M}_\odot < M_1$, which is consistent with our results. They use slightly different classifications of the fate of massive stars. In their fig. 29, they also classify electron capture SN with the criterion of $1.37\,{\rm M}_\odot < M_{\rm CO} < 1.43\,{\rm M}_\odot$ (see also Suwa et al. 2018, for core–collapse simulations in this mass range). In this paper, we do not focus on these kinds of SNe (see Fig. 2). They also consider pair-instability SN and pulsational pair-instability SN with certain criteria. Those SNe should appear in more massive stars, $M_{\rm ZAMS} > 50\,{\rm M}_\odot$, and does not affect our results. Note that in a higher mass range, $M_{\rm ZAMS} > 30\,{\rm M}_\odot$, the value of $M_{\rm CO}$ significantly depends on the mass-loss prescription of Wolf–Rayet stars (see also fig. 1 of Patton et al. 2022).

If a binary is close enough so that the binary interaction is effective, more complex behaviour is exhibited. In the parameter region of $10^{1.5}\,{\rm R}_\odot < a < 10^{3.5}\,{\rm R}_\odot$, a SN progenitor becomes a Type Ibc SN

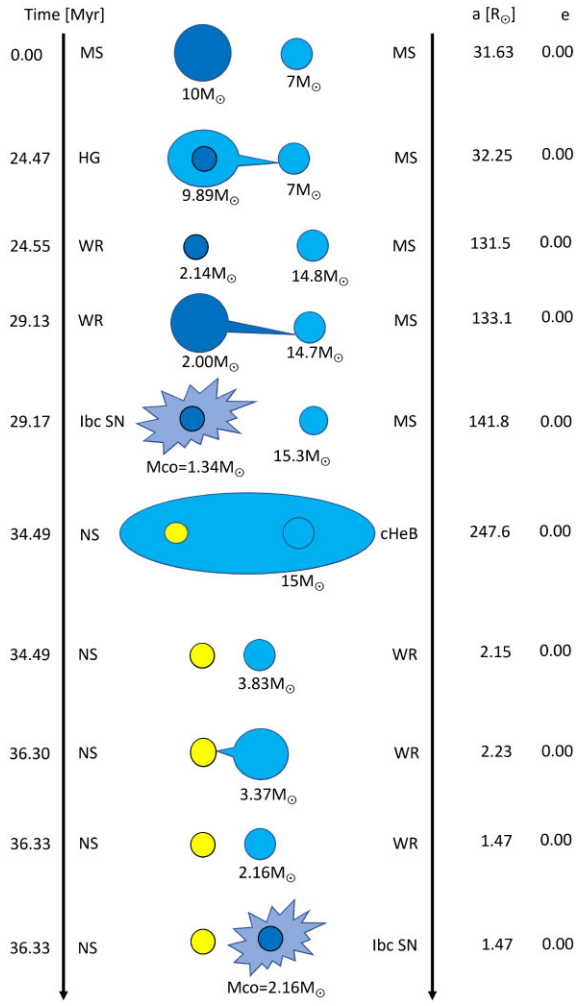

Figure 8. Example of the Type Ibc SN progenitor evolutionary path. MS, HG, WR, and cHeB are main sequence, Hertzsprung gap, Wolf–Rayet star, and helium core burning phase, respectively.

due to mass-loss by binary interactions. One typical evolutionary path of Type Ibc SN progenitors is shown in Fig. 8. Since the primary star and the secondary star lose their envelopes via mass transfer and common envelope phase, respectively, they can become type Ibc SN due to mass-loss. Another consequence is that binary effects reduce the $M_{\rm CO}$ of the primary; see Fig. 4 and compare $M_{\rm CO}$ in $10^{1.5}\,{\rm R}_\odot < a < 10^{3.5}\,{\rm R}_\odot$ to that in $10^{3.5}\,{\rm R}_\odot < a$. At $M_1 \sim 20\,{\rm M}_\odot$, $M_{\rm CO} \sim 2$–$3\,{\rm M}_\odot$ for $10^{1.5}\,{\rm R}_\odot < a < 10^{3.5}\,{\rm R}_\odot$ but $M_{\rm CO} \sim 5\,{\rm M}_\odot$ in $10^{3.5} < a$.

These results are consistent with Schneider et al. (2021). In their fig. 3, Case A and Case B mass transfer makes the core mass lighter. The effect of mass transfer on the secondary star is complicated. See Fig. 5, at $a \sim 10^3\,{\rm R}_\odot$ and $10\,{\rm M}_\odot < M_2 < 20\,{\rm M}_\odot$, the core mass is increased by the mass transfer from the primary star. In the region with smaller a and M_2, core mass is also increased due to the same reason. Note that the parameter regions of the figure are limited and correspond to the double in Fig. 1.

If a binary is close enough to merge, there are generally two main scenarios, depending on the evolutionary stage of the primary star. If the primary star has already become a compact object, the secondary star disappears through merging with the primary compact object. In the range $a \simeq 10^2\,{\rm R}_\odot$ to $a \simeq 10^3\,{\rm R}_\odot$, a massive binary where

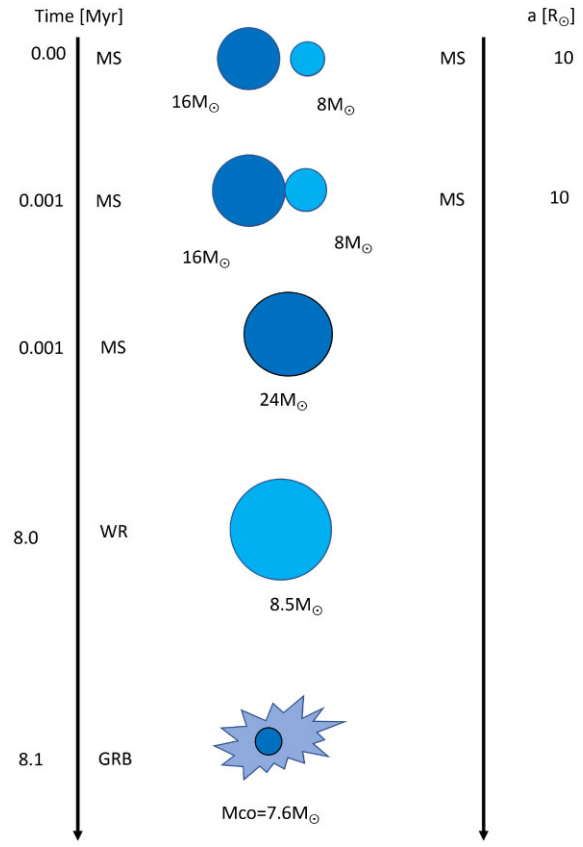

Figure 9. Example of the long GRB progenitor evolutionary path.

both stars were originally expected to undergo SNe therefore only experience one SN due to the merger. On the other hand, if the primary star is not a compact object, the merger creates a rapidly rotating star. The CO core of the merged remnant tend to be increased by the rotation effect. Subsequently, part or most of the angular momentum of the merged remnant can be lost by stellar wind mass-loss.

Merged remnants that lose their hydrogen envelope due to stellar winds while retaining sufficient angular momentum until the time of their explosion can lead to long GRBs. Note that Fragos et al. (2023) stop their simulation after the merger, and we cannot compare results. Long GRBs appear in a limited parameter range, $a = 10\,{\rm R}_\odot$ and $M_1 \sim 15\,{\rm M}_\odot$, as see in Fig. 2. We show the main channel for the birth of long GRB progenitors in Fig. 9. Typically, long GRB progenitors gain huge angular momenta from a binary merger. If the mass of the merged progenitors is relatively massive, angular momentum loss due to strong stellar wind mass prevents the occurrence of a long GRB. On the other hand, if the mass of merged progenitors is relatively low mass, they can evolve while retaining angular momentum until just before the gravitational collapse. Thus, systems whose mass $M_1 \sim 15\,{\rm M}_\odot$ can undergo gravitational collapse while retaining sufficient angular momentum of the CO core. If the merged progenitor mass is too low ($M_1 \lesssim 14\,{\rm M}_\odot$), they can collapse with a hydrogen envelope. In this case, the star is a giant with a large radius, causing the majority of the angular momentum to be held by the envelope rather than the CO core. Hence, not only is it unable to produce a long GRB, the angular momentum of the core also becomes significantly reduced (see Fig. 6).

We found two parameter regions for a rapidly rotating SN (Ibc-R), i.e. $(M_1,\ a) = (5\,{\rm M}_\odot,\ 10^{3.5}\,{\rm R}_\odot)$ in Fig. 2 and $(M_2,\ a) =$

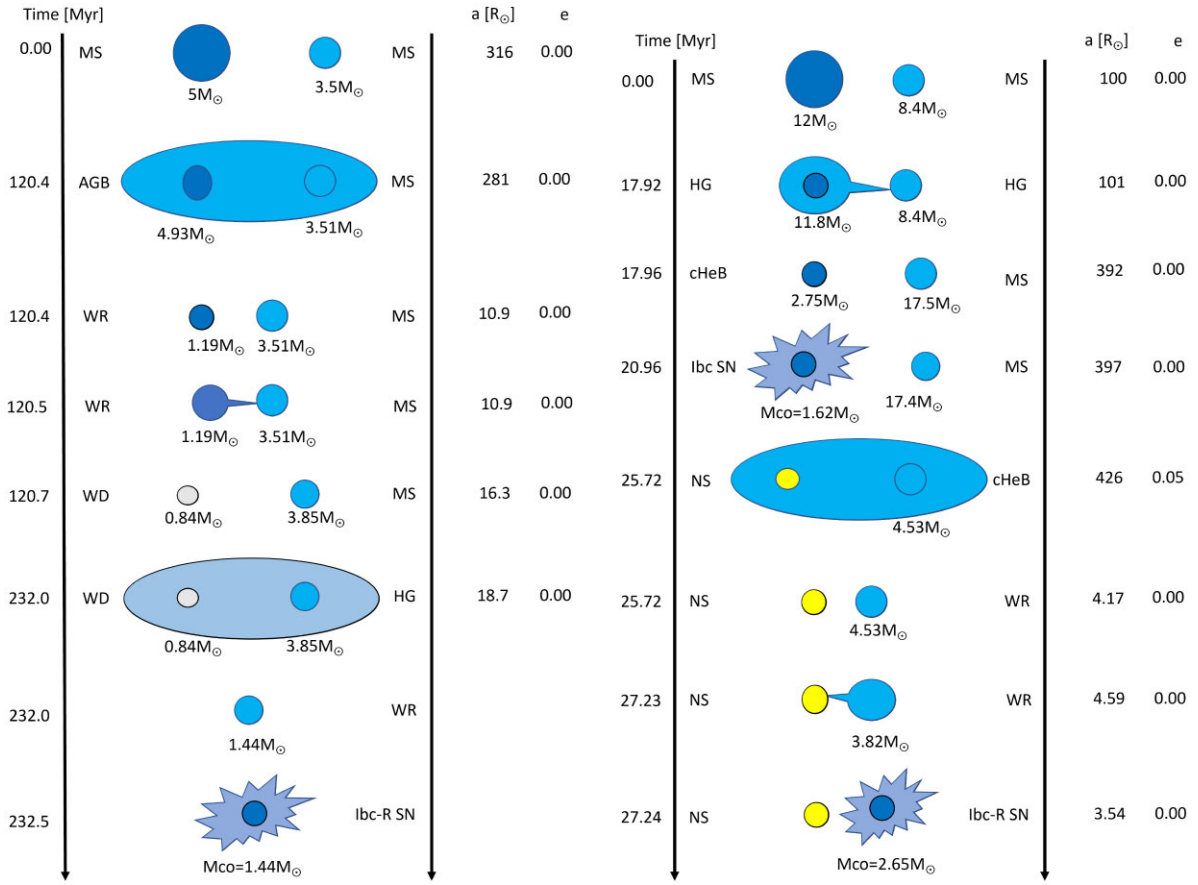

Figure 10. Examples of Ibc-R progenitor evolutionary paths. The case for $q = 0.7$ is shown. We have found another example as in Fig. B12 for $q = 0.9$.

($7\,M_\odot$, $10^2\,R_\odot$) in Fig. 3. We show the two pathways in Fig. 10. One of them is through a merger. For instance, in the left-hand side of Fig. 10, a binary system with an initial mass of $5M_\odot$ and an initial orbital semimajor axis of $a = 10^{2.5}\,R_\odot$ evolves into a binary system composed of a white dwarf (WD) and a red giant (RG). After the binary merger, the remaining Wolf–Rayet (WR) star undergoes a SN explosion. Because the binary merger allows for the retention of a significant amount of angular momentum, it can lead to a Ibc-R. In the right-hand side of Fig. 10, the second pathway involves the binary evolution leading to a very close binary system (a of a few $R_\odot$), such as a NS-WR binary, in the late stages. In this scenario, the secondary star undergoes rapid rotation due to tidal effects, and it eventually explodes as a Ibc-R. In both cases, the core mass is not so large, i.e. $M_{\rm CO} = 1.44\,M_\odot$ or $2.65\,M_\odot$. It is interesting to note that heavier stars are often employed in simulations, e.g. ($M_{\rm ZAMS}$, $M_{\rm CO}$) = ($27\,M_\odot$, $\sim 7\,M_\odot$) in Takiwaki et al. (2021); ($M_{\rm ZAMS}$, $M_{\rm CO}$) = ($35\,M_\odot$, 20–$30\,M_\odot$) in Obergaulinger & Aloy (2020). Although lighter stars are also considered ($M_{\rm ZAMS}$, $M_{\rm CO}$) = ($5\,M_\odot$, $4\,M_\odot$) in Obergaulinger & Aloy (2022), it is still heavier than what we observe due to binary effects.

There are two parameter regions corresponding to an AIC, see $(M_1, a) \sim (7\,M_\odot, 3000\,R_\odot)$ and $(9\,M_\odot, 30\,R_\odot)$ in Fig. 2. The two pathways are shown in Fig. 11. One of them is that the primary star, whose initial mass is lower than the SN criterion (in single stellar evolution case), becomes an AIC due to mass accretion from the secondary star. The other is the case where the primary star's initial mass is more massive than the SN criterion mass (in single stellar evolution case), but it loses a lot of mass via mass transfers and it cannot become a SN. However, it can become an AIC due to mass accretion from the secondary star. Interestingly, the angular momentum of the core is high in both case, see Fig. 6 and the points $(M_1, a) \sim (7\,M_\odot, 3000\,R_\odot)$, $(9\,M_\odot, 31.30\,R_\odot)$. Recently, simulations of AIC were performed (e.g. Mori et al. 2023) and the effect of rotation is considered (Abdikamalov et al. 2010; Longo Micchi, Radice & Chirenti 2023).

3.2 Population synthesis calculation

3.2.1 Initial parameter distribution and binary parameters

We conduct binary population synthesis calculations for 12 binary population models by varying the initial parameter distributions and binary evolution parameters with solar metallicity. The differences between the 12 binary population models are combinations of variations in the initial condition distribution of binary systems, mass transfer parameter β, and common envelope parameters $\alpha\lambda$. Table 2 shows the parameters for our 12 binary population models. For each model, we performed calculations for 10^5 binary systems.

Each initial condition model uses the same initial mass function (IMF) and the same initial mass ratio function (IMRF). We adopt the Salpeter IMF,

$$f(M) = M^{-2.35}, \tag{22}$$

from $3M_\odot$ to $100M_\odot$ Salpeter (1955), and the flat IMRF from Kobulnicky & Fryer (2007),

$$f(q) = \text{const}, \tag{23}$$

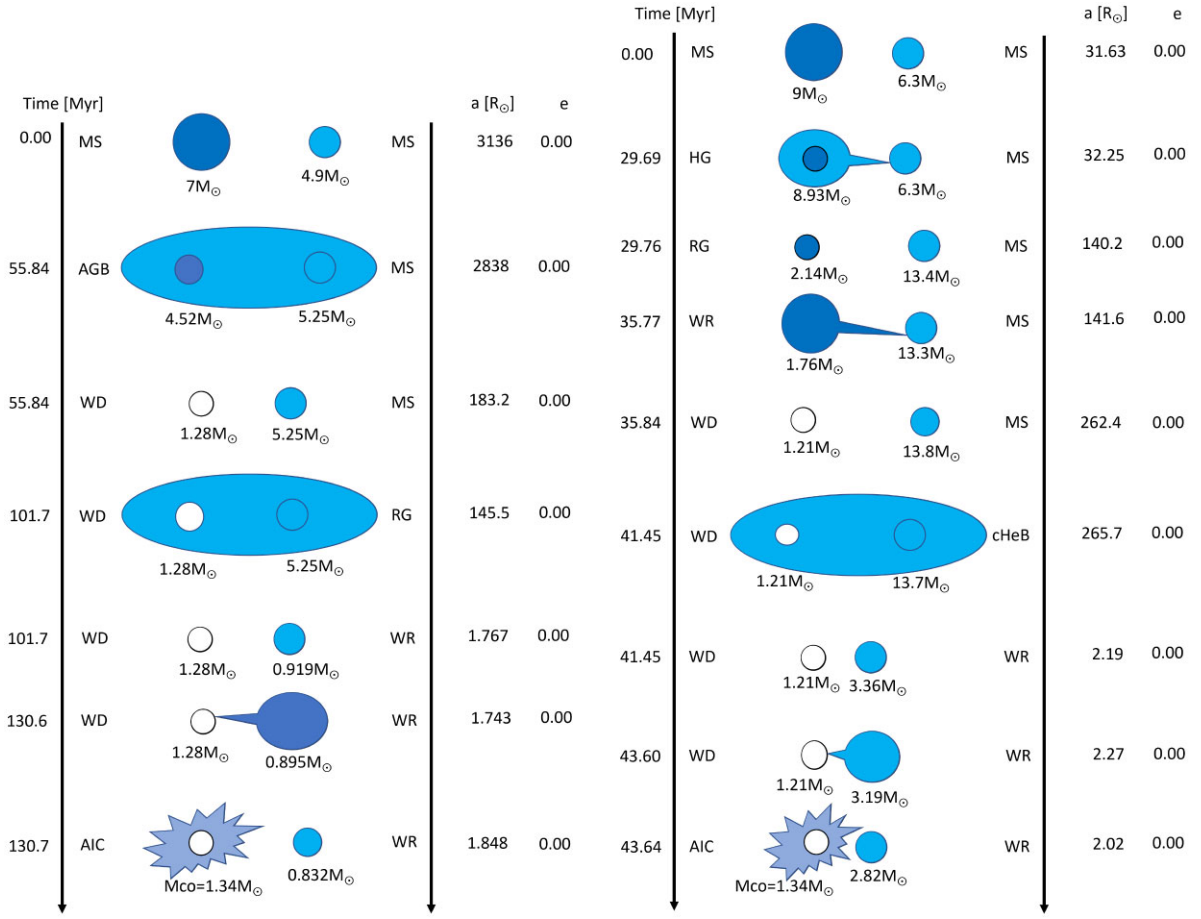

Figure 11. Examples of AIC progenitor evolutionary paths.

Table 2. Parameters for our 12 binary population synthesis models.

Model	Initial orbit population	β	$\alpha\lambda$
Sana_MT1_CE01	Sana et al. (2012)	1	0.1
Sana_MT05_CE01	Sana et al. (2012)	0.5	0.1
Sana_MT1_CE1	Sana et al. (2012)	1	1
Sana_MT05_CE1	Sana et al. (2012)	0.5	1
Sana_MT1_CE10	Sana et al. (2012)	1	10
Sana_MT05_CE10	Sana et al. (2012)	0.5	10
Abt_MT1_CE01	Heggie (1975); Abt (1983)	1	0.1
Abt_MT05_CE01	Heggie (1975); Abt (1983)	0.5	0.1
Abt_MT1_CE1	Heggie (1975); Abt (1983)	1	1
Abt_MT05_CE1	Heggie (1975); Abt (1983)	0.5	1
Abt_MT1_CE10	Heggie (1975); Abt (1983)	1	10
Abt_MT05_CE10	Heggie (1975); Abt (1983)	0.5	10

from 0 to 1, where $q = M_2/M_1$. In the case of the initial orbit parameter distributions such as separation (period) and eccentricity, we use two initial conditions. One is the initial orbit condition distributions from Sana et al. (2012). In order to calculate the separation in this model, we use the initial period P function,

$$f(\log P) = \left(\log\left[\frac{P}{\mathrm{day}}\right]\right)^{-0.55}, \tag{24}$$

from $\min[10^{0.15}\mathrm{d},\ P_{\min}]$ to $(P/\mathrm{day}) = 10^{3.5}$, where $P_{\min}$ is the minimum period where the binary does not interact, and use the initial eccentricity function,

$$f(e) = e^{-0.5}, \tag{25}$$

from 0 to 1. The other model adopts the orbital initial conditions by Heggie (1975) and Abt (1983). In this model, we use the log flat separation distribution,

$$f(a) = \frac{1}{a}, \tag{26}$$

from $a_{\min}$ to $10^6\mathrm{R}_\odot$, where $a_{\min}$ is the minimum separation where the binary does not interact, and use the initial eccentricity function

$$f(e) = e, \tag{27}$$

from 0 to 1.

For the mass transfer parameter β, we use 0.5 and 1. Here, $\beta = 1$ is a conservative mass transfer. On the other hand, $\beta = 0.5$ means that half of the transferred matter can be accreted to the companion star, and the rest is released out of the binary system.

We use 0.1, 1, and 10 as the combination of the common envelope parameters $\alpha\lambda$. When the common envelope parameter values are small, it means that there is less energy available to expel the envelope efficiently during the common envelope phase. As a result, the separation between the two stars tends to decrease because they remain closer together within the common envelope phase. Conversely, when the common envelope parameter values are large, it indicates that more energy is available to expel the envelope. This can lead to a more effective expulsion of the envelope, allowing

Table 3. The numbers of each SN type for our 12 models. The number of binaries per model is 10^5.

Model	AIC	Ibc	II	Ibc-R	BH	long GRB
Sana_MT1_CE01	31	6780	32 646	75	14 726	912
Sana_MT05_CE01	67	8940	28 986	155	11069	697
Sana_MT1_CE1	794	26 456	16 460	1298	11 412	729
Sana_MT05_CE1	263	22 542	14 785	1470	9183	524
Sana_MT1_CE10	438	26 322	12 015	1261	10 551	678
Sana_MT05_CE10	320	25 519	9449	1696	8266	488
Abt_MT1_CE01	214	2571	30 643	68	12 223	630
Abt_MT05_CE01	266	3195	30 089	60	11 417	594
Abt_MT1_CE1	458	11 239	24 728	563	10 121	421
Abt_MT05_CE1	341	10 211	24 054	549	9624	377
Abt_MT1_CE10	533	10 575	22 047	481	9544	382
Abt_MT05_CE10	464	10 186	21 450	457	9087	350

the two stars to separate further from each other after the common envelope phase.

3.2.2 *Results of population synthesis calculation*

Table 3 shows the results of our 12 binary population models, listing the numbers of each SN Type in 10^5 binaries. The main deference between the Sana initial orbit models and the Abt initail orbit models is the numbers of Type II and Type Ibc SNe. The fraction of close binaries is much higher in the Sana initial orbit models. Close binaries are more likely to become Type Ibc SNe and less likely to become Type II SNe (see Fig. 2). Thus, the number of Type Ibc SN is much higher in the Sana initial orbit models.

The mass transfer parameter β impacts strongly the number of AIC. Since AIC is caused by accretion, the small β which reduces the mass transfer generally makes binaries harder to become AIC.

The common envelope parameter $\alpha\lambda$ influences the number of mergers, with smaller $\alpha\lambda$ increasing binary mergers. Thus, there is a monotonic increases in the number of long GRB with small $\alpha\lambda$. However, for AIC and Ibc-R cases, the number of events peaks at $\alpha\lambda = 1$, and decrease both as $\alpha\lambda$ is decreased or increased. Particularly, at $\alpha\lambda = 0.1$, the number of events decreases significantly. This is because both AIC and Ibc-R scenarios require the binary separation to be reduced through a common envelope phase. When the primary star initiates the common envelope phase, and if $\alpha\lambda$ is too small, more binaries tend to merge at that stage. On the other hand, if $\alpha\lambda$ is too large, it does not shrinks the orbit much, leading to a slight decrease in the likelihood of forming close binary systems later on. The sharp increase in the number of Type II SNe and the sharp decrease in the number of Type Ibc SNe when $\alpha\lambda = 0.1$ are attributed to an increase in binaries that fail to effectively shed the envelope during the common envelope phase and consequently merge. After the merger, the presence of the remaining envelope makes it more likely for the star to become a Type II SN. In order to calculate the fractions of each SN type for our 12 binary population models, we assume a binary fraction f_b of 70 per cent (e.g. Sana et al. 2012) and $f_b = 50$ per cent (e.g. Tian et al. 2018). According to Fig. 2, for effectively single stars, relatively light stars ($8\,M_\odot < M < 20\,M_\odot$) tend to become Type II SN, while more massive stars ($> 20\,M_\odot$) tend to become BH. If $f_b = 70$ per cent (50 per cent), the number of Type II SN and the number of BH increase to 8163 (19 049) and 2959 (6903), respectively. Figs 12 and 13 show the fractions of each SN type for our 12 binary population models with f_b =70 per cent, and $f_b = 50$ per cent, respectively. The numerical data are provided in Appendix C. Observations of SN at low redshift reveal the fraction of SN types. Li et al. (2011), Shivvers et al. (2017), Perley et al. (2020), and Smith et al. (2020) show the fraction of II:Ibc = 75:25, 79.9:20.1, 72.2:27.8, and 76.6:23.4, respectively. We show in Figs 14 and 15 the fraction of SN Ibc and SN II to sum of them for each of our 12 binary population model with $f_b = 70$ per cent and $f_b = 50$ per cent, respectively.

Among the binary population models we calculated, the Abt_MT1_CE1 with $f_b = 70$ per cent and $f_b = 50$ per cent, the Abt_MT1_CE10 with $f_b = 70$ per cent and $f_b = 50$ per cent, the Abt_MT05_CE1 model with $f_b = 70$ per cent, and the Abt_MT05_CE10 model with $f_b = 70$ per cent are consistent with the observations (Li et al. 2011; Shivvers et al. 2017; Perley et al. 2020; Smith et al. 2020). Previous studies (e.g. De Donder & Vanbeveren 1998; Eldridge et al. 2013; Briel, Stevance & Eldridge

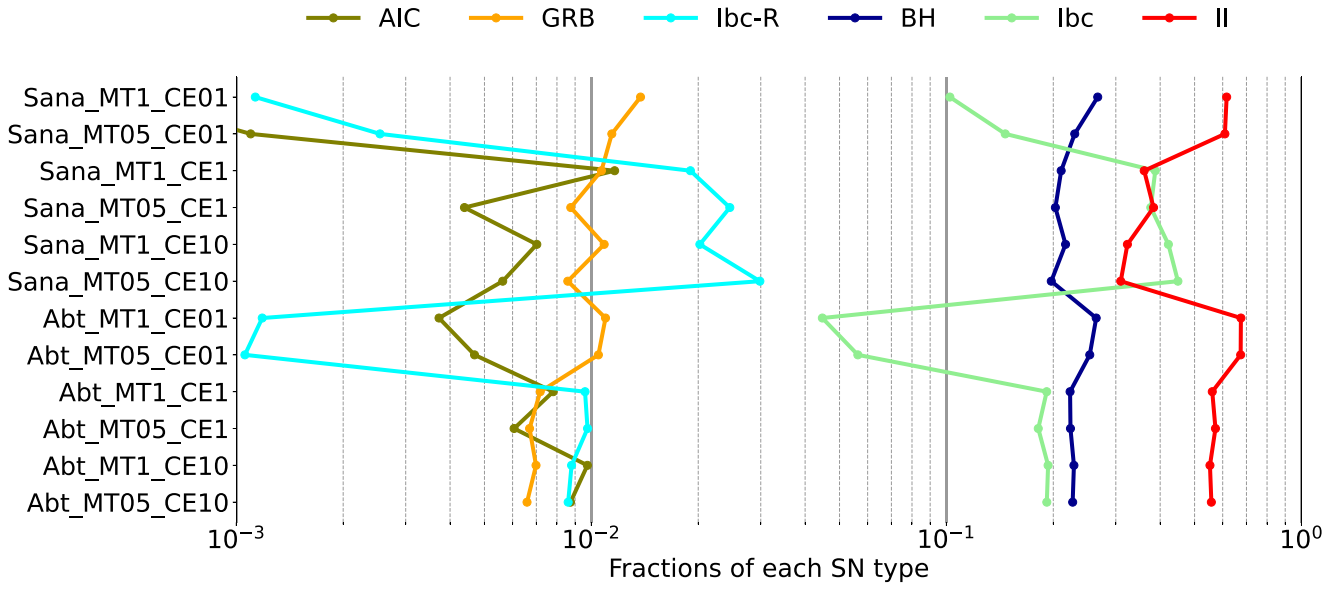

Figure 12. The fractions of each SN type for our 12 models, with binary fraction f_b =70 per cent.

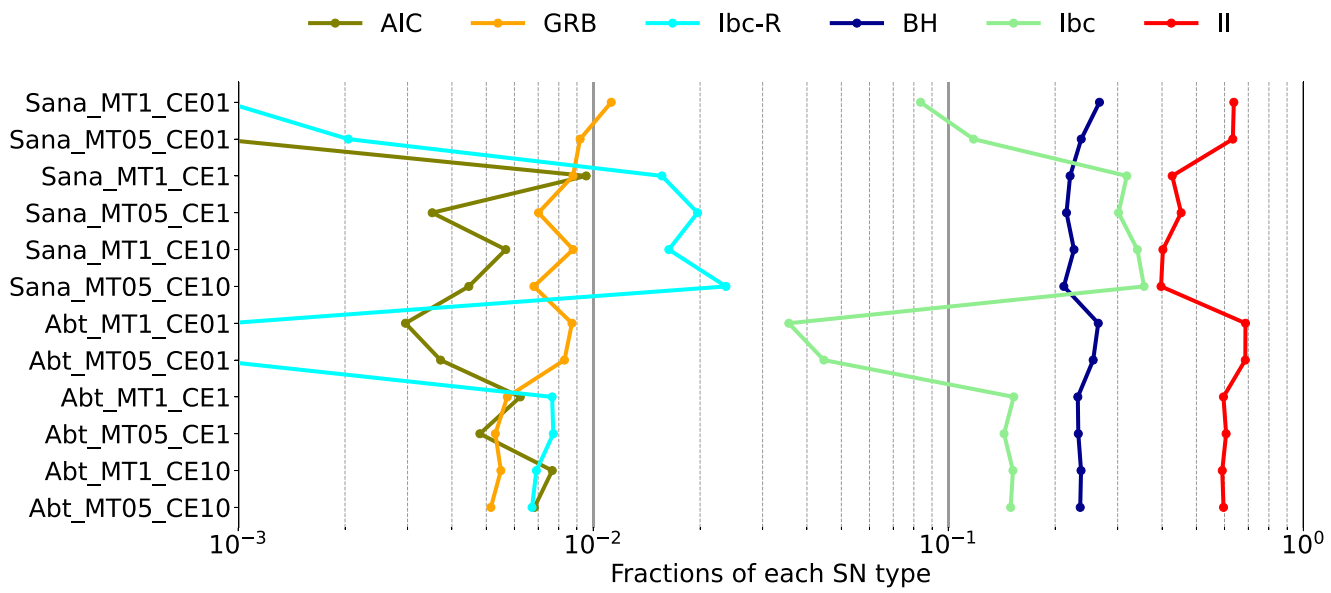

Figure 13. Same as Fig. 12 but with f_b =50 per cent.

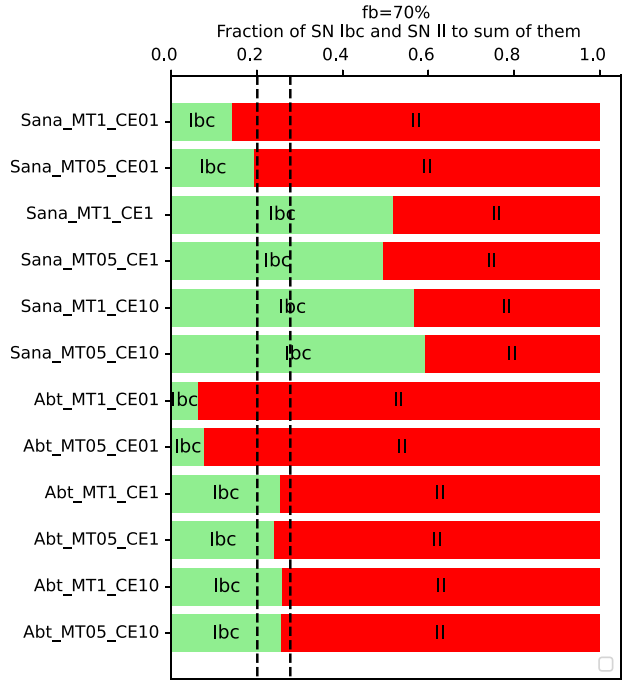

Figure 14. The fraction of Type Ibc SNe and Type II SNe to sum of them for each binary synthesis model with binary fraction $f_b = 70$ per cent. The black dashed lines shows the region of SNe fractions from observations (Li et al. 2011; Shivvers et al. 2017; Perley et al. 2020; Smith et al. 2020).

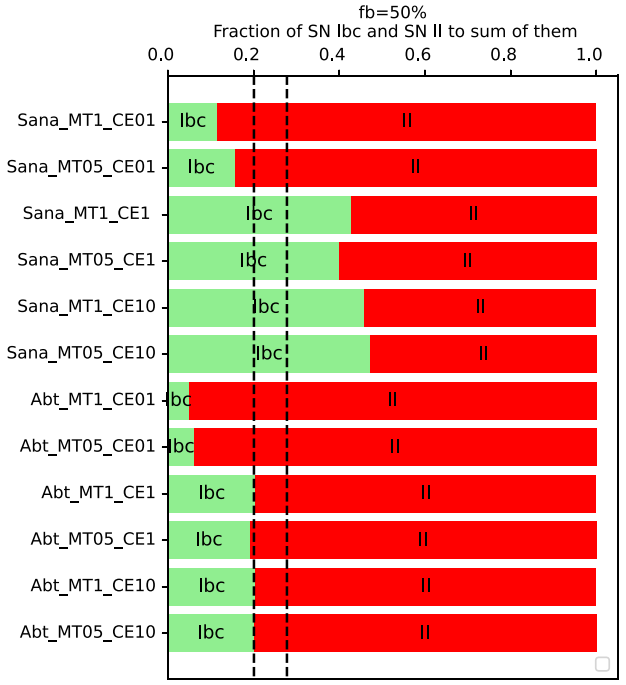

Figure 15. Same as Fig. 14 but for binary fraction $f_b = 50$ per cent.

2023) also show that the fractions of Ibc are around 70 per cent. De Donder & Vanbeveren (1998) also show that the this ratio strongly depend on the binary fraction as same as our result. In the binary population models using Sana et al. (2012) initial parameters, we find that due to a higher number of close binary systems, there is a tendency for more Type Ibc SNe compared to Type II SNe, in comparison to the models using Heggie (1975) and Abt (1983) initial parameters.

The local SN rate in our galaxy $R_{\rm SN}$ can be calculated as,

$$R_{\rm SN} = \frac{\int_3^{100} M^{-2.35}{\rm d}M}{\int_{0.08}^{0.5} M^{-1.3}{\rm d}M + \int_{0.5}^{100} M^{-2.35}{\rm d}M} \times \frac{N_{\rm Ibc} + N_{\rm II} + N_{\rm Ibc-R}}{2N_{\rm binary} + N_{\rm single}} \frac{{\rm SFR}_{\rm gal}}{\langle M \rangle}, \quad (28)$$

where $\langle M \rangle$, $N_{\rm Ibc}$, $N_{\rm II}$, and $N_{\rm Ibc-R}$ are the average stellar mass, the numbers of Type Ibc SN, Type II SN, and Ibc-R, respectively. We use the Kroupa IMF from $0.08{\rm M}_\odot$ to $0.5{\rm M}_\odot$ (Kroupa 2001). $N_{\rm binary}$ and $N_{\rm single}$ are the numbers of total binary systems and single star

systems, respectively. $\mathrm{SFR_{gal}}$ and $\langle M \rangle$ are the star formation late of our galaxy (assumed $2\,\mathrm{M_\odot\ yr^{-1}}$; Elia et al. 2022), and the average mass of stars, respectively. In our simulation, we find $R_{\rm SN}$ falls from 1.78×10^{-2} yr^{-1} to 2.47×10^{-2} yr^{-1}. These values are consistent with the core–collapse SN rate in our galaxy, $R_{\rm SN,obs} = 3.2^{+7.3}_{-2.6} \times 10^{-2}$ yr^{-1} (Adams et al. 2013).

The local long GRB rate at $z \sim 0$ can be calculated as,

$$R_{\rm GRB} = f_B \frac{\int_3^{100} M^{-2.35} {\rm d}M}{\int_{0.08}^{0.5} M^{-1.3} {\rm d}M + \int_{0.5}^{100} M^{-2.35} {\rm d}M} \times \frac{N_{\rm GRB}}{2N_{\rm binary} + N_{\rm single}} \frac{\rm SFR}{\langle M \rangle}, \quad (29)$$

where f_B, $N_{\rm GRB}$, and SFR are the beaming factor of long GRB ($f_B = 0.01$ estimated in Liang et al. 2008; Kinugawa & Asano 2017; Kinugawa et al. 2019), the number of long GRB, and the star formation rate at $z \sim 0$ (SFR $= 10^{-1.82}$ estimated in Wyder et al. 2005; Madau & Dickinson 2014), respectively. We find that the long GRB rate of our models is from $7.94 \left(\frac{f_B}{0.01}\right)$ yr^{-1} Gpc^{-3} to $25.6 \left(\frac{f_B}{0.01}\right)$ yr^{-1} Gpc^{-3}. Note that GRB rate strongly depends on the beaming factor, so we explicitly stated the value of the beaming factor used in our calculations. On the one hand, the local long GRB rate from observation is $1.3^{+0.6}_{-0.7}$ yr^{-1} Gpc^{-3} (Wanderman & Piran 2010), much lower than our estimates. On the other hand, observations suggest that there are many long GRBs with lower luminosities that are harder to detect (Pian et al. 2006), and the long GRB rate $1.3^{+0.6}_{-0.7}$ yr^{-1} Gpc^{-1} (Wanderman & Piran 2010) only includes the 'normal' long GRBs with high luminosity $L > 10^{49}$ ergs s^{-1}. The low luminosity long GRB rate is estimated $R_{\rm LLGRB} \sim 100$–600 yr^{-1} Gpc^{-1} (Pian et al. 2006; Liang et al. 2007). If we assume that all long GRB progenitors of our models become a low luminosity long GRB, then we estimated the low luminosity long GRB rate from $56.7 \left(\frac{f_B}{1/14}\right)$ yr^{-1} Gpc^{-1} to $182 \left(\frac{f_B}{1/14}\right)$ yr^{-1} Gpc^{-1} using a beaming factor for low luminosity long GRB $f_B = 1/14$ (Liang et al. 2007). According to Liang et al. (2007), it is possible that f_B of a low luminosity long GRB is greater than 1/14. In this case, this rate could become even larger. Thus, the low luminosity long GRB rates of our models are roughly consistent with the low luminosity long GRB rate from observations.

Based on our population synthesis models, we are able to estimate the rates of Ibc-R and AIC. To the best of our knowledge, this is the first time for the Ibc-R rate to be estimated. Shibagaki et al. (2020) assume long GRB rates as a proxy for the rate and we confirm that assumption is not wrong. In the best-fitting models (Abt_MT05_CE10 model or Abt_MT1_CE1 model), the rate is close to the long GRB rate. Though it is a rare opportunity, we can expect neutrino and gravitational waves from nearby Ibc-R, which would have time-variability of the frequency of proto-neutron star (e.g. Takiwaki et al. 2021). Note that the rate strongly depends on the common envelope parameter. As discussed above, in the models with $\alpha\lambda = 0.1$, the rate significantly drops. The rate of AIC is similar to Ibc-R.

We can also obtain the NS:BH ratios from our calculations. In all models, the NS:BH fraction remains relatively constant, ranging from 79:21 to 72:28. These values are approximately the same as a single star case (NS:BH = 73:27) if we assume that progenitors with $8\,\mathrm{M_\odot} \leq M \leq 20\,\mathrm{M_\odot}$ become type II SNe (NSs) and progenitors with $20\,\mathrm{M_\odot} < M$ become BHs. These are broadly consistent with observations. In particular, there are a few candidate massive stars that have disappeared without obvious luminous SNe (Gerke, Kochanek & Stanek 2015; Adams et al. 2017a,b; Basinger et al. 2021; Neustadt et al. 2021). If these collapse to black holes, they can be combined with the number of disappearances coincident with SNe to yield the fraction of core collapses that fail to produce SNe (Kochanek et al. 2008). Current estimates of such a black hole channel is $23.6^{+23.3}_{-15.7}$ per cent of massive stars undergoing collapse. Other indirect probes also indicate similar fractions (e.g. Horiuchi et al. 2014).

4 SUMMARY AND DISCUSSION

In this paper, we systematically investigate how binary interactions affect the progenitors of SNe. To this end, we first conducted binary evolution calculations with fixed mass ratios. With this setup, we explored the orbital separations and primary star masses where various types of SNe can be produced, and delineated the evolutionary pathways through which each SN explosion could occur. We found that binaries with orbital separation greater than the red giant radius evolve similarly to single stars. Relatively lighter stars in such binaries become Type II SNe, while heavier stars become BHs. On the other hand, we found that binaries with orbital separations roughly equal to or less than the red giant's radius develop into diverse types of SNe due to binary interactions, such as a common envelope phase and/or stable mass transfer. Rare explosion phenomenon such as rapidly rotating SNe and AIC are also observed in this separation range, $10^{1.5}\,\mathrm{R_\odot} < a < 10^{3.5}\,\mathrm{R_\odot}$ with lighter mass progenitor $M_{\rm ZAMS} < 9\,\mathrm{M_\odot}$. Furthermore, we found that binaries with orbital separation $\lesssim 10\,\mathrm{R_\odot}$ undergo stellar mergers before core collapse. This implies that such progenitor stars have relatively large angular momentum at core collapse, making them conducive as long GRB progenitors.

In a previous study, Kinugawa & Asano (2017) calculated the long GRB rate of binary merger progenitor models (Fryer & Heger 2005). In their binary merger progenitor model, the stellar merger of naked He stars or the stellar mergers of naked He star and red giant as the long GRB progenitor were considered. Kinugawa & Asano (2017) showed that the long GRB rate by the binary merger progenitor model is consistent with the long GRB rate from observation (Wanderman & Piran 2010), and the metallicity evolution effect to the binary merger progenitor model can explain the evolution of the redshift of the long GRB rate. In our study, however, there is no long GRB progenitor of the binary merger progenitor model. The reason for this difference lies in the different treatments of the envelopes of the remnants that merged during the common envelope phase. In Kinugawa & Asano (2017), it was assume that all the envelope will evaporate after the common envelope phase due to the huge angular momentum by the merger. On the other hand, we assumed that the envelope is not completely blown away during the common envelope phase, and partially remains. The binary merger progenitor model considers the merging of He stars in the late stages of evolution, which implies that they might have more angular momentum compared to our model, where stars merge early in the main sequence and lose angular momentum due to stellar winds. Furthermore, the binary merger progenitor model calculation (Kinugawa & Asano 2017) is consistent with the normal long GRB rate, whereas our calculation models appear to be consistent with low luminosity long GRBs rather than normal long GRBs. Therefore, it is plausible that the formation processes of normal long GRBs and low luminosity long GRBs are different.

This paper only considers the solar metallicity cases. As the first of a series of papers considering binary effects on SN progenitors, here we focus on surveys of the initial binary parameter space of supernova progenitors, such as initial primary mass and initial separation. We

will calculate low metallicity cases in the next paper. For example, De Donder & Vanbeveren (2003), Eldridge et al. (2008), Eldridge et al. (2011), and Briel et al. (2022) show that the SN rate and the ratios of different SNe depend on the metallicity of progenitors. Furthermore, long GRBs, including low luminosity long GRBs, explode in low metallicity environments (e.g. Modjaz et al. 2008; Graham & Fruchter 2017; Palmerio et al. 2019), and binary evolution studies (Kinugawa & Asano 2017; Kinugawa et al. 2019; Briel et al. 2022) also suggest that the long GRB rate strongly depends on the metallicity. Thus we expect that the low luminosity long GRB rate in the low metallicity case would be much higher than in the solar metallicity case, because the low metallicity progenitors are easier to retain their angular momentum due to weak wind mass-loss. The low luminosity long GRB rate in our study is close to the observed low luminosity long GRB rate, but the value of our study is almost the same as the lower limit of observation. Thus, the low luminosity long GRB rate from binary evolution using low metallicity stars might be more consistent with the observation result compared to the solar metallicity case in this paper.

We show the examples of SNe and GRB evolutionary paths in Figs 8, 9, 10, 11, and B12 in the parameter survey. In 100 000 binary evolutionary calculations, we demonstrate the proportions of these evolutionary paths among each SN type, using the Abt_MT1_CE1 model as an example.

In the case of Ibc SN, it was found that both stars in binary systems follow the Ibc SN evolution pathway like Fig. 8 in approximately 3 per cent of cases. The most common evolution pathway, accounting for 41 per cent of Ibc SN cases, involves a merger event followed by an Ibc SN ('merger' in Fig. 1). Additionally, there is a pathway (9 per cent of Ibc SN cases) where stars in the mass range that would not naturally undergo SN explosions due to rotational effects after the merger ['merger(rotation)']. This result is attributed to the formation of many close binary systems due to the initial distribution of binaries in our population synthesis calculation, resulting in a higher occurrence of mergers during the giant phase due to binary interaction effects such as common envelope phase. Another pathway (32 per cent of Ibc SN cases) involves only the primary star exploding as an Ibc supernova while the companion star does not explode ('single'). Although Section 2 provided an example for the case of a mass ratio of 0.7, the binary population synthesis calculation for 100 000 binaries revealed a higher frequency of cases where the mass of the companion star is smaller. There is a pathway where both the primary and companion stars undergo SNe ('double'), but the primary star becomes a type II SN, black hole, or undergoes AIC, etc., while only the companion star becomes a type Ibc SN, accounting for 2 per cent of the cases. Furthermore, there is a pathway (13 per cent of Ibc SN cases) where both stars in the binary system also explode ('double'), but only the primary star becomes an Ibc SN while the companion star becomes a supernova other than Ibc (mainly Type II SN). This occurrence is due to the effect of pulsar kicks, which was ignored in Section 2 for simplicity. Including this effect resulted in the disruption of the binary system, with only the primary star being affected by binary interactions to become an Ibc SN, while the companion star, being disrupted by the kick, subsequently undergoes a Type II SN without experiencing binary interactions. Our results, indicating a significant proportion of SNe without a companion star due to mergers or disruption by kicks, are consistent with observational findings suggesting that more than half of the SNe at the birth of a neutron star are not in binary systems (e.g. Kochanek 2021, 2023).

In the case of long GRB, 'merger' channels as shown in Fig. 9 account for 96 per cent of the total. Additionally, among binaries, there are cases where only the primary star produces a long GRB while the companion star triggers other supernova explosions ('double'), constituting 3 per cent, and cases where only the primary star produces a long GRB while the companion star remains inactive ('single'), constituting 1 per cent.

For Ibc-R SNe, as shown in the left side of Fig. 10, there are cases where the primary star, which would not normally undergo SN, becomes an Ibc-R SN due to the rotational effect of binary merger ['merger(rotation)'], accounting for 83 per cent of the cases. On the right side of Fig. 10, there are instances where the primary star undergoes a SN first, then becomes a close binary, with the tidal effect causing the companion star to spin up and result in an Ibc-R SN ('double'), comprising 4 per cent of the cases. As shown in Fig. B12, when the masses of the primary and companion stars are similar, there is a scenario where the primary star becomes an Ibc-R supernova through binary interaction-induced spin-up, accounting for 8 per cent of the cases. In these instances, both scenarios of spin-up through mass accretion as depicted in Fig. B12 and spin-up through tidal effects are considered.

In the case of AIC, all evolutionary paths involve AIC via mass accretion onto a WD, as shown in Fig. 11, and there are no paths involving merger. The majority (85 per cent) of cases involve the primary star becoming a WD and undergoing AIC through accretion, while the companion star does not undergo a supernova ('single'), most of which are driven by primary stars in the mass range that would not naturally undergo a SN, as depicted in the left side of Fig. 11. In cases where the primary star becomes a WD due to binary interaction in the mass range that would naturally undergo a SN, and subsequently undergoes AIC through accretion, the companion star usually triggers a SN due to mass transfer from the primary star ('double'), accounting for 15 per cent of the cases, as depicted in the right side of Fig. 11.

In our calculations, close binaries tend to lead to Type Ibc SNe. Therefore, the models with Sana et al. (2012) initial parameters typically showed larger discrepancies in the ratio between Type Ibc and Type II SNe compared to observations, with an overabundance of Type Ibc SNe. While this can be offset with a lower common envelope parameter, which results in increased number of remnants merging within the common envelope and a significant increase in the number of Type II SNe, this outcome is highly dependent on the handling of the envelopes of the merging remnants in the process. If we assume the same hypothesis of Kinugawa & Asano (2017), the number of Type II SNe could decrease in this case. To increase the number of Type II SNe in the Sana et al. (2012) initial parameter models, several factors might be needed, e.g. an increase in the number of single stars, an increase in binaries with significantly wider separations where interactions do not play a significant role, or making the stripping of the hydrogen envelope by common envelope interactions less effective than it is now.

Binary population models like ours holds various possible applications. For example, there are growing numbers of observations of neutron stars (see Enoto, Kisaka & Shibata 2019, and references therein). Previous studies have revealed valuable insights into the distributions of mass, rotation, magnetic fields, and kicks (e.g. Noutsos et al. 2013; Igoshev et al. 2022). Though this paper does not discuss neutron star properties, it is important to compare our theoretical models with observations. Recently, the correlation of neutron star spins and spin-kick alignment is discussed in Janka, Wongwathanarat & Kramer (2022).

Also, since we calculate the number of explosive phenomena and CO core mass of the progenitor, our models allow for an updated

prediction of DSNB flux such as previously demonstrated in Horiuchi et al. (2021). The DSNB is a promising method to investigate the properties of extragalactic core collapses (Beacom 2010; Lunardini 2016; Ando et al. 2023). The SuperKamiokande (SK) water Cherenkov detector has already excluded some theoretical models and placed upper bounds on the DSNB flux (Abe et al. 2021). Recently, SK was upgraded with a gadolinium salt (SK-Gd), and expected to perform significantly more sensitive searches for the DSNB (Harada et al. 2023). On the theoretical side, more realistic predictions of DNSB is ongoing. For example, Horiuchi et al. (2021) and Kresse, Ertl & Janka (2021) consider the binary effect. Ashida & Nakazato (2022) considers the DSNB as a probe to investigate the stellar collapse fate. Ashida, Nakazato & Tsujimoto (2023) uses a new modelling of galactic chemical evolution, where a variable stellar initial mass function depending on the galaxy type. Ekanger et al. (2022) explore multiple schemes to estimate time-integrated spectra, while Ekanger et al. (2024) employs the neutrino spectrum calculated in 2D long-term simulations and updated star formation data.

In this study, we simply connected the CO core mass to the fate of the core collapse. However other parameters could be important to determine the ultimate fate, i.e. explodability and mass of the compact objects (Pejcha & Thompson 2015; Ertl et al. 2016; Tsang, Vartanyan & Burrows 2022; Wang et al. 2022; Takahashi, Takiwaki & Yoshida 2023). For improvements, systematic studies of core–collapse SNe could extend previous works in 1D simulations (O'Connor & Ott 2011; Ugliano et al. 2012; Sukhbold et al. 2016; Couch, Warren & O'Connor 2020; Ebinger et al. 2020; Boccioli, Mathews & O'Connor 2021), 2D simulations (Nakamura et al. 2015; Summa et al. 2016; Vartanyan & Burrows 2023), and 3D simulations (Burrows et al. 2020). Simultaneously, more sophisticated input physics should be required, e.g. neutrino oscillation (Ehring et al. 2023; Nagakura 2023), neutrino reaction rate (Kotake et al. 2018; Sugiura et al. 2022), and equation of state (Fischer et al. 2014, 2020). For lighter progenitors, more systematic stellar evolution models in advanced stage are required to determine the appropriate range of CO core mass which leads to AIC and electron capture supernovae (Takahashi, Yoshida & Umeda 2013; Doherty et al. 2015; Poelarends et al. 2017; Wu & Wang 2018; Leung & Nomoto 2019; Leung, Nomoto & Suzuki 2020; Limongi et al. 2024). Those may not correspond to minimum mass neutron stars (Suwa et al. 2018). Using such data, we can develop a better phenomenological treatment of the explosions (e.g. Belczynski et al. 2012).

There is much room for improvement in the assumptions used in this study. Even in the physics used in single star evolution we have uncertainties. For example, we have several recipes of wind mass-loss rate (de Jager, Nieuwenhuijzen & van der Hucht 1988; Nugis & Lamers 2000; Vink, de Koter & Lamers 2000, 2001; Vink & de Koter 2005), thereby impacting the core mass (e.g. Woosley, Sukhbold & Janka 2020). Advanced stages of stellar evolution lack strict constraints on overshooting parameters (e.g. Yoshida et al. 2019; Temaj et al. 2024) necessitating high-resolution simulations of convective shells for accurate determination (Cristini et al. 2017). We use REACLIB for the reaction rate of nucleosynthesis (Cyburt et al. 2010), but uncertainties with some reaction channels potentially alter stellar structures (e.g. Takahashi et al. 2016). The final stellar structure can also depend on numerical resolution (e.g. Kato, Hirai & Nagakura 2020). Angular momentum transport inside stars requires much theoretical efforts. The Tayler–Spruit dynamo is usually assumed (e.g. Heger et al. 2005) and wave-driven mechanism is also considered (Fuller et al. 2015). On binary star evolution, there are uncertainties about the mass transfer rate and the angular momentum loss (Hirai 2023; Willcox et al. 2023). Recently, calculations using binary population synthesis calculations and MESA have been conducted to study the stability of mass transfer (e.g. Gallegos-Garcia et al. 2021; Marchant et al. 2021; Klencki et al. 2022; Briel et al. 2023; Temmink et al. 2023; Dorozsmai & Toonen 2024). Particularly, in Temmink et al. (2023), the stability of mass transfer for post-main sequence stars with masses ranging from $1M_\odot$ to $8\ M_\odot$ has been investigated. According to their results, the threshold mass ratio q_{cri} for the formation of a common envelope when $q = M_a/M_d < q_{cri}$ is approximately 0.25 during the Hertzsprung gap phase and around 1 during the red giant phase, gradually decreasing in subsequent evolution, where M_a and M_d are the mass of the accreter and the mass of the donor. While our adopted criterion value is approximately 0.25 for the Hertzsprung gap phase, it increases to around 1.3 for the red giant phase, making common envelope formation more likely. Since their calculations consider stars with masses up to $8M_\odot$, it is necessary to investigate how much difference arises in our calculations, which handle massive stars that become supernovae. Additionally, in the formation of binary black hole mergers, differences between population synthesis and MESA simulations have been observed in whether binary black holes with black hole and helium star companions undergo common envelope evolution, leading to significant differences in the merger rate and the period at formation of binary black holes in each calculation (Gallegos-Garcia et al. 2021). Recent observations have shed light on the dependence of binary initial distributions and binary rates on parameters such as initial mass and orbital separation (Moe & Di Stefano 2017). Consequently, there is a growing need for binary evolution calculations that take these dependencies into account.

Despite these uncertainties, we have been able to explore the progenitors behind major as well as rare SN types, and moreover their typical evolutionary paths. To make progress, it would be necessary to start from our study and systematically consider each uncertain factor, comparing and evaluating them in relation to observations one by one.

ACKNOWLEDGEMENTS

We thank the anonymous referee, K. Takahashi, R. Hirai, and C. Lunardini for informative discussions which improved the discussions in the paper. This work was supported by the Research Institute of Stellar Explosive Phenomena at Fukuoka University and also by JSPS KAKENHI Grant Number (JP21K13915, JP22K03630, JP23H04899, JP23K25895, JP23K20848, JP23K22494, JP23K03400, and JP24K00631). The work of SH is also supported by the U.S. Department of Energy Office of Science under award number DE-SC0020262, and U.S. National Science Foundation Grant No. AST1908960 and No. PHY-2209420. This work was supported by World Premier International Research Center Initiative (WPI Initiative), MEXT, Japan. This research was also supported by MEXT as 'Program for Promoting researches on the Supercomputer Fugaku' (Structure and Evolution of the Universe Unraveled by Fusion of Simulation and AI; Grant Number JPMXP1020230406) and JICFuS.

DATA AVAILABILITY

The data underlying this article will be shared on reasonable request to the corresponding author.

REFERENCES

Abdikamalov E. B., Ott C. D., Rezzolla L., Dessart L., Dimmelmeier H., Marek A., Janka H. T., 2010, Phys. Rev. D, 81, 044012
Abe K. et al., 2021, Phys. Rev. D, 104, 122002
Abt H. A., 1983, ARA&A, 21, 343
Adams S. M., Kochanek C. S., Beacom J. F., Vagins M. R., Stanek K. Z., 2013, ApJ, 778, 164
Adams S. M., Kochanek C. S., Gerke J. R., Stanek K. Z., Dai X., 2017a, MNRAS, 468, 4968
Adams S. M., Kochanek C. S., Gerke J. R., Stanek K. Z., 2017b, MNRAS, 469, 1445
Aguilera-Dena D. R., Langer N., Moriya T. J., Schootemeijer A., 2018, ApJ, 858, 115
Ando S., Ekanger N., Horiuchi S., Koshio Y., 2023, in Proceedings of the Japan Academy, Series B. preprint (arXiv:2306.16076)
Ashida Y., Nakazato K., 2022, ApJ, 937, 30
Ashida Y., Nakazato K., Tsujimoto T., 2023, ApJ, 953, 151
Basinger C. M., Kochanek C. S., Adams S. M., Dai X., Stanek K. Z., 2021, MNRAS, 508, 1156
Beacom J. F., 2010, Annu. Rev. Nucl. Part. Sci., 60, 439
Belczynski K., Kalogera V., Bulik T., 2002, ApJ, 572, 407
Belczynski K., Bulik T., Heger A., Fryer C., 2007, ApJ, 664, 986
Belczynski K., Kalogera V., Rasio F. A., Taam R. E., Zezas A., Bulik T., Maccarone T. J., Ivanova N., 2008, ApJS, 174, 223
Belczynski K., Wiktorowicz G., Fryer C. L., Holz D. E., Kalogera V., 2012, ApJ, 757, 91
Boccioli L., Mathews G. J., O'Connor E. P., 2021, ApJ, 912, 29
Bogomazov A. I., Popov S. B., 2009, Astron. Rep., 53, 325
Bollig R., Yadav N., Kresse D., Janka H.-T., Müller B., Heger A., 2021, ApJ, 915, 28
Breivik K. et al., 2020, ApJ, 898, 71
Briel M. M., Eldridge J. J., Stanway E. R., Stevance H. F., Chrimes A. A., 2022, MNRAS, 514, 1315
Briel M. M., Stevance H. F., Eldridge J. J., 2023, MNRAS, 520, 5724
Bugli M., Guilet J., Foglizzo T., Obergaulinger M., 2023, MNRAS, 520, 5622
Burrows A., Radice D., Vartanyan D., Nagakura H., Skinner M. A., Dolence J. C., 2020, MNRAS, 491, 2715
Cantiello M., Yoon S. C., Langer N., Livio M., 2007, A&A, 465, L29
Chatzopoulos E., Frank J., Marcello D. C., Clayton G. C., 2020, ApJ, 896, 50
Chieffi A., Limongi M., 2020, ApJ, 890, 43
Chini R., Hoffmeister V. H., Nasseri A., Stahl O., Zinnecker H., 2012, MNRAS, 424, 1925
Chrimes A. A., Stanway E. R., Eldridge J. J., 2020, MNRAS, 491, 3479
Cigan P. et al., 2019, ApJ, 886, 51
Conroy C., 2013, ARA&A, 51, 393
Couch S. M., Chatzopoulos E., Arnett W. D., Timmes F. X., 2015, ApJ, 808, L21
Couch S. M., Warren M. L., O'Connor E. P., 2020, ApJ, 890, 127
Cristini A., Meakin C., Hirschi R., Arnett D., Georgy C., Viallet M., Walkington I., 2017, MNRAS, 471, 279
Cyburt R. H. et al., 2010, ApJS, 189, 240
De Donder E., Vanbeveren D., 1998, A&A, 333, 557
De Donder E., Vanbeveren D., 2003, New Astron., 8, 817
de Jager C., Nieuwenhuijzen H., van der Hucht K. A., 1988, A&AS, 72, 259
De Marco O., Izzard R. G., 2017, Publ. Astron. Soc. Austr., 34, e001
Doherty C. L., Gil-Pons P., Siess L., Lattanzio J. C., Lau H. H. B., 2015, MNRAS, 446, 2599
Dominik M., Belczynski K., Fryer C., Holz D. E., Berti E., Bulik T., Mandel I., O'Shaughnessy R., 2013, ApJ, 779, 72
Dorozsmai A., Toonen S., 2024, MNRAS, 530, 3706
Ebinger K., Curtis S., Ghosh S., Fröhlich C., Hempel M., Perego A., Liebendörfer M., Thielemann F.-K., 2020, ApJ, 888, 91
Eggleton P. P., 1983, ApJ, 268, 368
Eggleton P., 2011, Evolutionary Processes in Binary and Multiple Stars. Cambridge Univ. Press, Cambridge
Ehring J., Abbar S., Janka H.-T., Raffelt G., Tamborra I., 2023, Phys. Rev. D, 107, 103034
Ekanger N., Horiuchi S., Kotake K., Sumiyoshi K., 2022, Phys. Rev. D, 106, 043026
Ekanger N., Horiuchi S., Nagakura H., Reitz S., 2024, Phys. Rev. D, 109, 023024
Ekström S. et al., 2012, A&A, 537, A146
Eldridge J. J., Maund J. R., 2016, MNRAS, 461, L117
Eldridge J. J., Stanway E. R., 2022, ARA&A, 60, 455
Eldridge J. J., Izzard R. G., Tout C. A., 2008, MNRAS, 384, 1109
Eldridge J. J., Langer N., Tout C. A., 2011, MNRAS, 414, 3501
Eldridge J. J., Fraser M., Smartt S. J., Maund J. R., Crockett R. M., 2013, MNRAS, 436, 774
Elia D. et al., 2022, ApJ, 941, 162
Enoto T., Kisaka S., Shibata S., 2019, Rep. Prog. Phys., 82, 106901
Ertl T., Janka H. T., Woosley S. E., Sukhbold T., Ugliano M., 2016, ApJ, 818, 124
Fields C. E., 2022, ApJ, 924, L15
Fischer T., Hempel M., Sagert I., Suwa Y., Schaffner-Bielich J., 2014, Eur. Phys. J. A, 50, 46
Fischer T., Wu M.-R., Wehmeyer B., Bastian N.-U. F., Martínez-Pinedo G., Thielemann F.-K., 2020, ApJ, 894, 9
Fragos T. et al., 2023, ApJS, 264, 45
Fryer C. L., Heger A., 2005, ApJ, 623, 302
Fryer C. L., Belczynski K., Wiktorowicz G., Dominik M., Kalogera V., Holz D. E., 2012, ApJ, 749, 91
Fujibayashi S., Sekiguchi Y., Shibata M., Wanajo S., 2023, ApJ, 956, 100
Fuller J., Cantiello M., Lecoanet D., Quataert E., 2015, ApJ, 810, 101
Gallegos-Garcia M., Berry C. P. L., Marchant P., Kalogera V., 2021, ApJ, 922, 110
Gehrels N., Ramirez-Ruiz E., Fox D. B., 2009, ARA&A, 47, 567
Georgy C., Ekström S., Meynet G., Massey P., Levesque E. M., Hirschi R., Eggenberger P., Maeder A., 2012, A&A, 542, A29
Gerke J. R., Kochanek C. S., Stanek K. Z., 2015, MNRAS, 450, 3289
Giacobbo N., Mapelli M., Spera M., 2017, MNRAS, 474, 2959
Graham J. F., Fruchter A. S., 2017, ApJ, 834, 170
Harada M. et al., 2023, ApJ, 951, L27
Heger A., Langer N., Woosley S. E., 2000, ApJ, 528, 368
Heger A., Fryer C. L., Woosley S. E., Langer N., Hartmann D. H., 2003, ApJ, 591, 288
Heger A., Woosley S. E., Spruit H. C., 2005, ApJ, 626, 350
Heggie D. C., 1975, MNRAS, 173, 729
Hijikawa K., Kinugawa T., Yoshida T., Umeda H., 2019, ApJ, 882, 93
Hirai R., 2023, MNRAS, 523, 6011
Hirai R., Sato T., Podsiadlowski P., Vigna-Gómez A., Mandel I., 2020, MNRAS, 499, 1154
Hjellming M. S., 1989, PhD thesis, Illinois Univ. at Urbana-Champaign, Savoy.
Horiuchi S., Nakamura K., Takiwaki T., Kotake K., Tanaka M., 2014, MNRAS, 445, L99
Horiuchi S., Kinugawa T., Takiwaki T., Takahashi K., Kotake K., 2021, Phys. Rev. D, 103, 043003
Hsieh H.-F., Cabezón R., Ma L.-T., Pan K.-C., 2024, ApJ, 961, 194
Huang W., Gies D. R., McSwain M. V., 2010, ApJ, 722, 605
Hurley J. R., Pols O. R., Tout C. A., 2000, MNRAS, 315, 543
Hurley J. R., Tout C. A., Pols O. R., 2002, MNRAS, 329, 897
Hut P., 1981, A&A, 99, 126
Igoshev A. P., Frantsuzova A., Gourgouliatos K. N., Tsichli S., Konstantinou L., Popov S. B., 2022, MNRAS, 514, 4606
Ivanova N., Belczynski K., Kalogera V., Rasio F. A., Taam R. E., 2003, ApJ, 592, 475
Iwakami W., Nagakura H., Yamada S., 2014, ApJ, 793, 5
Janka H.-T., Wongwathanarat A., Kramer M., 2022, ApJ, 926, 9
Kato C., Hirai R., Nagakura H., 2020, MNRAS, 496, 3961
Keszthelyi Z., 2023, Galaxies, 11, 40
Kinugawa T., Asano K., 2017, ApJ, 849, L29
Kinugawa T., Inayoshi K., Hotokezaka K., Nakauchi D., Nakamura T., 2014, MNRAS, 442, 2963

Kinugawa T., Miyamoto A., Kanda N., Nakamura T., 2016, MNRAS, 456, 1093
Kinugawa T., Harikane Y., Asano K., 2019, ApJ, 878, 128
Kinugawa T., Nakamura T., Nakano H., 2020, MNRAS, 498, 3946
Kinugawa T., Nakamura T., Nakano H., 2021a, MNRAS, 501, L49
Kinugawa T., Nakamura T., Nakano H., 2021b, MNRAS, 504, L28
Kinugawa T., Nakamura T., Nakano H., 2021c, Prog. Theor. Exp. Phys., 2021, 021E01
Klencki J., Istrate A., Nelemans G., Pols O., 2022, A&A, 662, A56
Kobulnicky H. A., Fryer C. L., 2007, ApJ, 670, 747
Kobulnicky H. A. et al., 2014, ApJS, 213, 34
Kochanek C. S., 2021, MNRAS, 507, 5832
Kochanek C. S., 2023, MNRAS, 519, 3865
Kochanek C. S., Beacom J. F., Kistler M. D., Prieto J. L., Stanek K. Z., Thompson T. A., Yuksel H., 2008, ApJ, 684, 1336
Kotake K., Takiwaki T., Fischer T., Nakamura K., Martínez-Pinedo G., 2018, ApJ, 853, 170
Kresse D., Ertl T., Janka H.-T., 2021, ApJ, 909, 169
Kroupa P., 2001, MNRAS, 322, 231
Kuroda T., Arcones A., Takiwaki T., Kotake K., 2020, ApJ, 896, 102
Langer N., 2012, ARA&A, 50, 107
Laplace E., Justham S., Renzo M., Götberg Y., Farmer R., Vartanyan D., de Mink S. E., 2021, A&A, 656, A58
Larsson J. et al., 2023, ApJ, 949, L27
Leung S.-C., Nomoto K., 2019, Publ. Astron. Soc. Austr., 36, e006
Leung S.-C., Nomoto K., Suzuki T., 2020, ApJ, 889, 34
Li W. et al., 2011, MNRAS, 412, 1441
Liang E., Zhang B., Virgili F., Dai Z. G., 2007, ApJ, 662, 1111
Liang E.-W., Racusin J. L., Zhang B., Zhang B.-B., Burrows D. N., 2008, ApJ, 675, 528
Limongi M., 2017, in Alsabti A., Murdin P., eds, Supernovae from Massive Stars. Springer International Publishing, Cham, p. 513
Limongi M., Roberti L., Chieffi A., Nomoto K., 2024, ApJS, 270, 29
Longo Micchi L. F., Radice D., Chirenti C., 2023, MNRAS, 525, 6359
Lovegrove E., Woosley S. E., Zhang W., 2017, ApJ, 845, 103
Lubow S. H., Shu F. H., 1975, ApJ, 198, 383
Lunardini C., 2016, Astropart. Phys., 79, 49
Madau P., Dickinson M., 2014, ARA&A, 52, 415
Maeder A., 2009, Physics, Formation and Evolution of Rotating Stars. Springer, Berlin
Marchant P., Pappas K. M. W., Gallegos-Garcia M., Berry C. P. L., Taam R. E., Kalogera V., Podsiadlowski P., 2021, A&A, 650, A107
Mason B. D., Hartkopf W. I., Gies D. R., Henry T. J., Helsel J. W., 2009, AJ, 137, 3358
Matsumoto J., Asahina Y., Takiwaki T., Kotake K., Takahashi H. R., 2022, MNRAS, 516, 1752
McNeill L. O., Müller B., 2022, MNRAS, 509, 818
Menon A., Heger A., 2017, MNRAS, 469, 4649
Mocák M., Meakin C., Campbell S. W., Arnett W. D., 2018, MNRAS, 481, 2918
Modjaz M. et al., 2008, AJ, 135, 1136
Moe M., Di Stefano R., 2017, ApJS, 230, 15
Mori M., Sawada R., Suwa Y., Tanikawa A., Kashiyama K., Murase K., 2023, preprint (arXiv:2306.17381)
Müller B., Heger A., Liptai D., Cameron J. B., 2016a, MNRAS, 460, 742
Müller B., Viallet M., Heger A., Janka H.-T., 2016b, ApJ, 833, 124
Müller B., Gay D. W., Heger A., Tauris T. M., Sim S. A., 2018, MNRAS, 479, 3675
Nagakura H., 2023, Phys. Rev. Lett., 130, 211401
Nakamura K., Takiwaki T., Kuroda T., Kotake K., 2015, PASJ, 67, 107
Nakamura K., Takiwaki T., Kotake K., 2022, MNRAS, 514, 3941
Neustadt J. M. M., Kochanek C. S., Stanek K. Z., Basinger C. M., Jayasinghe T., Garling C. T., Adams S. M., Gerke J., 2021, MNRAS, 508, 516
Nomoto K., Kobayashi C., Tominaga N., 2013, ARA&A, 51, 457
Noutsos A., Schnitzeler D. H. F. M., Keane E. F., Kramer M., Johnston S., 2013, MNRAS, 430, 2281
Nugis T., Lamers H. J. G. L. M., 2000, A&A, 360, 227
O'Connor E., Ott C. D., 2011, ApJ, 730, 70
Obergaulinger M., Aloy M. Á., 2020, MNRAS, 492, 4613
Obergaulinger M., Aloy M. Á., 2022, MNRAS, 512, 2489
Obergaulinger M., Janka H. T., Aloy M. A., 2014, MNRAS, 445, 3169
Ogata M., Okawa H., Fujisawa K., Yasutake N., Yamamoto Y., Yamada S., 2023, MNRAS, 521, 2561
Ono M., Nagataki S., Ferrand G., Takahashi K., Umeda H., Yoshida T., Orlando S., Miceli M., 2020, ApJ, 888, 111
Palmerio J. T. et al., 2019, A&A, 623, A26
Patton R. A., Sukhbold T., 2020, MNRAS, 499, 2803
Patton R. A., Sukhbold T., Eldridge J. J., 2022, MNRAS, 511, 903
Pejcha O., Thompson T. A., 2015, ApJ, 801, 90
Perley D. A. et al., 2020, ApJ, 904, 35
Peters P. C., 1964, Phys. Rev., 136, 1224
Peters P. C., Mathews J., 1963, Phys. Rev., 131, 435
Pian E. et al., 2006, Nature, 442, 1011
Poelarends A. J. T., Wurtz S., Tarka J., Cole Adams L., Hills S. T., 2017, ApJ, 850, 197
Popov S. B., Prokhorov M. E., 2006, MNRAS, 367, 732
Rasio F. A., Tout C. A., Lubow S. H., Livio M., 1996, ApJ, 470, 1187
Riley J. et al., 2022, ApJS, 258, 34
Salpeter E. E., 1955, ApJ, 121, 161
Sana H. et al., 2012, Science, 337, 444
Sana H. et al., 2013, A&A, 550, A107
Schneider F. R. N., Podsiadlowski P., Müller B., 2021, A&A, 645, A5
Sekiguchi Y., Shibata M., 2011, ApJ, 737, 6
Shibagaki S., Kuroda T., Kotake K., Takiwaki T., 2020, MNRAS, 493, L138
Shibagaki S., Kuroda T., Kotake K., Takiwaki T., Fischer T., 2024, MNRAS, 531, 3732
Shivvers I. et al., 2017, PASP, 129, 054201
Smartt S. J., 2009, ARA&A, 47, 63
Smith N., 2014, ARA&A, 52, 487
Smith K. W. et al., 2020, PASP, 132, 085002
Spera M., Mapelli M., Giacobbo N., Trani A. A., Bressan A., Costa G., 2019, MNRAS, 485, 889
Stanway E. R., Eldridge J. J., 2018, MNRAS, 479, 75
Sugiura K., Furusawa S., Sumiyoshi K., Yamada S., 2022, Prog. Theor. Exp. Phys., 2022, 113E01
Sukhbold T., Ertl T., Woosley S. E., Brown J. M., Janka H. T., 2016, ApJ, 821, 38
Sukhbold T., Woosley S. E., Heger A., 2018, ApJ, 860, 93
Summa A., Hanke F., Janka H.-T., Melson T., Marek A., Müller B., 2016, ApJ, 825, 6
Summa A., Janka H.-T., Melson T., Marek A., 2018, ApJ, 852, 28
Suwa Y., Yoshida T., Shibata M., Umeda H., Takahashi K., 2018, MNRAS, 481, 3305
Taam R. E., Sandquist E. L., 2000, ARA&A, 38, 113
Takahashi K., Langer N., 2021, A&A, 646, A19
Takahashi K., Yoshida T., Umeda H., 2013, ApJ, 771, 28
Takahashi K., Umeda H., Yoshida T., 2014, ApJ, 794, 40
Takahashi K., Yoshida T., Umeda H., Sumiyoshi K., Yamada S., 2016, MNRAS, 456, 1320
Takahashi K., Takiwaki T., Yoshida T., 2023, ApJ, 945, 19
Takiwaki T., Kotake K., Foglizzo T., 2021, MNRAS, 508, 966
Tanikawa A., Yoshida T., Kinugawa T., Takahashi K., Umeda H., 2020, MNRAS, 495, 4170
Tauris T. M. et al., 2017, ApJ, 846, 170
Temaj D., Schneider F. R. N., Laplace E., Wei D., Podsiadlowski P., 2024, A&A, 682, A123
Temmink K. D., Pols O. R., Justham S., Istrate A. G., Toonen S., 2023, A&A, 669, A45
Tian Z.-J. et al., 2018, Res. Astron. Astrophys., 18, 052
Tsang B. T. H., Vartanyan D., Burrows A., 2022, ApJ, 937, L15
Ugliano M., Janka H.-T., Marek A., Arcones A., 2012, ApJ, 757, 69
Ulrich R. K., Burger H. L., 1976, ApJ, 206, 509
Umeda H., Nomoto K., 2008, ApJ, 673, 1014
Umeda H., Yoshida T., Takahashi K., 2012, Prog. Theor. Exp. Phys., 2012, 01A302

Urushibata T., Takahashi K., Umeda H., Yoshida T., 2018, MNRAS, 473, L101
Utrobin V. P., Wongwathanarat A., Janka H. T., Müller E., Ertl T., Menon A., Heger A., 2021, ApJ, 914, 4
Varma V., Müller B., 2021, MNRAS, 504, 636
Varma V., Müller B., Schneider F. R. N., 2023, MNRAS, 518, 3622
Vartanyan D., Burrows A., 2023, MNRAS, 526, 5900
Vartanyan D., Laplace E., Renzo M., Götberg Y., Burrows A., de Mink S. E., 2021, ApJ, 916, L5
Vink J. S., de Koter A., 2005, A&A, 442, 587
Vink J. S., de Koter A., Lamers H. J. G. L. M., 2000, A&A, 362, 295
Vink J. S., de Koter A., Lamers H. J. G. L. M., 2001, A&A, 369, 574
Wanderman D., Piran T., 2010, MNRAS, 406, 1944
Wang T., Vartanyan D., Burrows A., Coleman M. S. B., 2022, MNRAS, 517, 543
Webbink R. F., 1984, ApJ, 277, 355
Willcox R., MacLeod M., Mandel I., Hirai R., 2023, ApJ, 958, 138
Wolff S. C., Strom S. E., Dror D., Lanz L., Venn K., 2006, AJ, 132, 749
Woosley S. E., Bloom J. S., 2006, ARA&A, 44, 507
Woosley S. E., Heger A., 2006, ApJ, 637, 914
Woosley S. E., Heger A., 2007, Phys. Rep., 442, 269
Woosley S. E., Langer N., Weaver T. A., 1995, ApJ, 448, 315
Woosley S. E., Heger A., Weaver T. A., 2002, Rev. Mod. Phys., 74, 1015
Woosley S. E., Sukhbold T., Janka H. T., 2020, ApJ, 896, 56
Wu C.-Y., Wang B., 2018, Res. Astron. Astrophys., 18, 036
Wyder T. K. et al., 2005, ApJ, 619, L15
Yadav N., Müller B., Janka H. T., Melson T., Heger A., 2020, ApJ, 890, 94
Yoon S. C., Langer N., Norman C., 2006, A&A, 460, 199
Yoshida T., Suwa Y., Umeda H., Shibata M., Takahashi K., 2017, MNRAS, 471, 4275
Yoshida T., Takiwaki T., Kotake K., Takahashi K., Nakamura K., Umeda H., 2019, ApJ, 881, 16
Yoshida T., Takiwaki T., Aguilera-Dena D. R., Kotake K., Takahashi K., Nakamura K., Umeda H., Langer N., 2021a, MNRAS, 506, L20
Yoshida T., Takiwaki T., Kotake K., Takahashi K., Nakamura K., Umeda H., 2021b, ApJ, 908, 44
Zahn J. P., 1975, A&A, 41, 329
Zahn J. P., 1977, A&A, 500, 121
Zapartas E. et al., 2017, A&A, 601, A29

APPENDIX A: BINARY INTERACTIONS FOR SPIN AND ORBIT

A1 Tidal interaction

Tidal interaction changes the orbit and the spins of the binary system. There are two mechanisms for the dissipation of the tidal kinetic energy. One mechanism is the convective damping on the equilibrium tide for the stars with an outer convection envelope such as red giants. The other mechanism is the radiative damping on the dynamical tide for the stars with an outer radiative zone (Zahn 1977). The time evolution of the separation, the eccentricity, and the spin are calculated as

$$\frac{\mathrm{d}a}{\mathrm{d}t} = -6\frac{k}{T}q(1+q)\left(\frac{R_i}{a}\right)^8 \frac{a}{(1-e^2)^{\frac{15}{2}}} \times \left[f_1(e^2) - (1-e^2)^{\frac{3}{2}} f_2(e^2)\frac{\Omega_{\mathrm{spin},i}}{\Omega_{\mathrm{orb}}}\right], \quad \text{(A1)}$$

$$\frac{\mathrm{d}e}{\mathrm{d}t} = -27\frac{k}{T}q(1+q)\left(\frac{R_i}{a}\right)^8 \frac{e}{(1-e^2)^{\frac{13}{2}}} \times \left[f_3(e^2) - \frac{11}{18}(1-e^2)^{\frac{3}{2}} f_4(e^2)\frac{\Omega_{\mathrm{spin},i}}{\Omega_{\mathrm{orb}}}\right], \quad \text{(A2)}$$

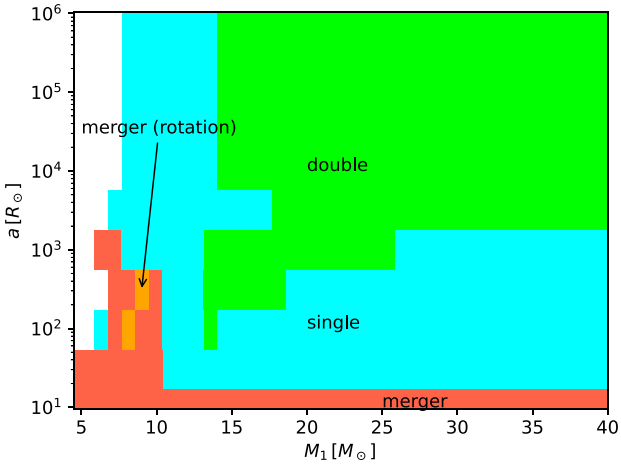

Figure A1. The binary progenitors of SNe in the $q = 0.5$ case.

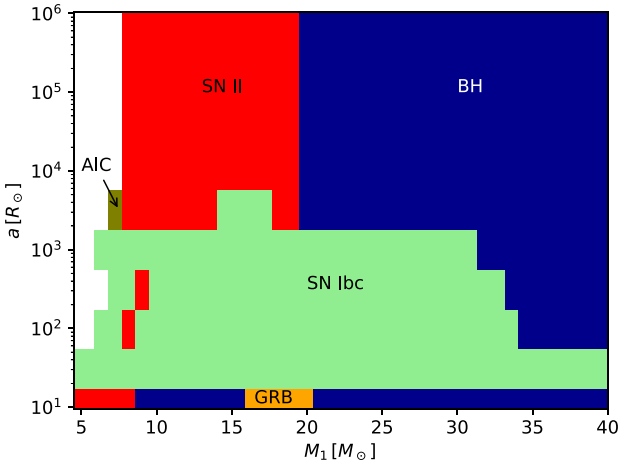

Figure A2. SN type of primary star in the $q = 0.5$ case.

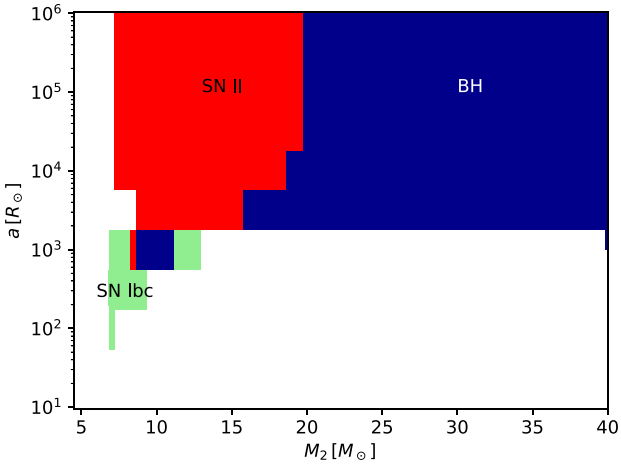

Figure A3. SN type of secondary star in the $q = 0.5$ case.

$$\frac{\mathrm{d}\Omega_{\mathrm{spin},i}}{\mathrm{d}t} = 3\frac{k}{T}\frac{q^2}{r_g^2}\left(\frac{R_i}{a}\right)^6 \frac{\Omega_{\mathrm{orb}}}{(1-e^2)^6} \times \left[f_2(e^2) - (1-e^2)^{\frac{3}{2}} f_5(e^2)\frac{\Omega_{\mathrm{spin},i}}{\Omega_{\mathrm{orb}}}\right], \quad \text{(A3)}$$

where

$$f_1(e^2) = 1 + \frac{31}{2}e^2 + \frac{255}{8}e^4 + \frac{185}{16}e^6 + \frac{25}{64}e^8, \quad \text{(A4)}$$

$$f_2(e^2) = 1 + \frac{15}{2}e^2 + \frac{45}{8}e^4 + \frac{5}{16}e^6, \quad \text{(A5)}$$

$$f_3(e^2) = 1 + \frac{15}{4}e^2 + \frac{15}{8}e^4 + \frac{5}{64}e^6, \quad \text{(A6)}$$

$$f_4(e^2) = 1 + \frac{3}{2}e^2 + \frac{1}{8}e^4, \quad \text{(A7)}$$

$$f_5(e^2) = 1 + 3e^2 + \frac{3}{8}e^4, \quad \text{(A8)}$$

where k/T, q, R_i, $\Omega_{\mathrm{spin},i}$, Ω_{orb}, and r_g are the coupling parameter depending on the tidal interaction mechanism, the mass ratio, the radius of the star, the spin angular velocity of the star, the angular velocity of the orbit, and the dimensionless gyration radius of the star, respectively (Zahn 1977; Hut 1981). Notation i means 1 (primary star) or 2 (secondary star).

If the star is a red giant, the convective damping of the equilibrium tide is effective. In this case, k/T is calculated as

$$\frac{k}{T} = \frac{2}{21}\frac{f_{\mathrm{con}}}{\tau_{\mathrm{con}}}\frac{M_{\mathrm{env},i}}{M_{\mathrm{i}}}, \quad \text{(A9)}$$

where $M_{\mathrm{env},i}$, f_{con}, and τ_{con} are the stellar envelope mass, the correction factor of the tidal torque, and the eddy turnover timescale (e.g. Rasio et al. 1996; Hurley et al. 2002), respectively. They are calculated as

$$\tau_{\mathrm{con}} = \left[\frac{M_{\mathrm{env},i}R_{\mathrm{env},i}\left(R_i - \frac{1}{2}R_{\mathrm{env},i}\right)}{3L_i}\right]^{1/3}, \quad \text{(A10)}$$

$$f_{\mathrm{con}} = \min\left[1, \left(\frac{\pi|\Omega_{\mathrm{orb}} - \Omega_{\mathrm{spin},i}|^{-1}}{\tau_{\mathrm{con}}}\right)^2\right], \quad \text{(A11)}$$

where L_i and $R_{\mathrm{env},i}$ are the stellar luminosity and the radius of the stellar envelope, respectively.

On the other hand, if the star have the radiative envelope i.e. the evolution stage is not a red giant, the tidal mechanism is the radiative damping of the dynamical tide (Zahn 1975). k/T is

$$\frac{k}{T} = 4.3118\times10^{-8}\left(\frac{M_i}{\mathrm{M}_\odot}\right)\left(\frac{R_i}{\mathrm{R}_\odot}\right)^2 \times \left(\frac{a}{1\,\mathrm{AU}}\right)^{-5}(1+q)^{5/6}E_2\ \mathrm{yr}^{-1}, \quad \text{(A12)}$$

where E_2 is the tidal coefficient factor (Zahn 1977; Hurley et al. 2002).

A2 Magnetic braking

When a rotating star loses its mass, magnetic braking removes angular momentum from the rotating star via a magnetic field. The spin angular momentum loss by the magnetic braking is

$$\dot{J}_{\mathrm{spin},i} = -5.83\times10^{-16}\frac{M_{\mathrm{env},i}}{M_i}\left(R_i\Omega_{\mathrm{spin},i}\right)^3\mathrm{M}_\odot\mathrm{R}_\odot^2\mathrm{yr}^{-2}, \quad \text{(A13)}$$

where masses and the radius are in solar units and Ω_{spin} in units of years (Hurley et al. 2000; Hurley et al. 2002).

A3 Gravitational radiation

After the stars in a binary explode or collapse at the end of their lifetime, the compact star binary is formed. The compact binary loses the angular momentum and the orbital energy by the gravitational radiation. We use the weak-field approximation formalism given by Peters & Mathews (1963) and Peters (1964). The loss of angular momentum, the orbital separation, and the eccentricity are described as

$$\frac{j}{J} = -\frac{32G^3M_1M_2M_{\mathrm{total}}}{5c^5a^4}\frac{1+\frac{7}{8}e^2}{\left(1-e^2\right)^{5/2}}, \quad \text{(A14)}$$

$$\frac{\dot{a}}{a} = -\frac{64G^3M_1M_2M_{\mathrm{total}}}{5c^5a^4}\frac{1+\frac{73}{24}e^2+\frac{37}{96}e^4}{\left(1-e^2\right)^{7/2}} \quad \text{(A15)}$$

and

$$\frac{\dot{e}}{e} = -\frac{304G^3M_1M_2M_{\mathrm{total}}}{15c^5a^4}\frac{1+\frac{121}{304}e^2}{\left(1-e^2\right)^{5/2}}. \quad \text{(A16)}$$

APPENDIX B: PARAMETER SURVEY OF Q = 0.5, AND 0.9 CASES

We show the parameter dependence of SN types, CO core mass, and angular momentum in the mass ratio of $q = 0.5$ and $q = 0.9$ while the case for $q = 0.7$ is discussed in Section 3.1.

B1 q = 0.5 case

Fig. A1 shows the progenitor of the SN in the mass ratio $q = 0.5$. Figs A2 and A3 show the fate of the primary star and the secondary star, respectively, as a function of their ZAMS mass and binary separation. Figs B1 and B2 show CO core mass as a function of their ZAMS mass and binary separation. Figs B3 and B4 show the angular momentum as a function of their ZAMS mass and binary separation.

The one of the main differences between this case and the $q = 0.7$ case is the absence of a pathway leading to Ibc-R. See points $(M_1, a) = (8\,\mathrm{M}_\odot, 100\,\mathrm{R}_\odot)$, and $(9\,\mathrm{M}_\odot, 10^{2.5}\,\mathrm{R}_\odot)$ in Fig. A2, they collapse via merger (rotation). These progenitors evolve via a similar evolution path of Ibc-R progenitor in the $q = 0.7$ case (left-hand side of Fig. 10). However, in these cases, the hydrogen envelopes remain

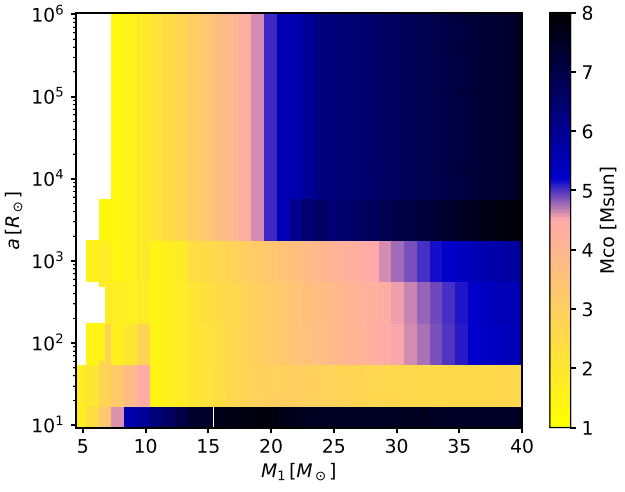

Figure B1. CO core mass of primary star in the $q = 0.5$ case.

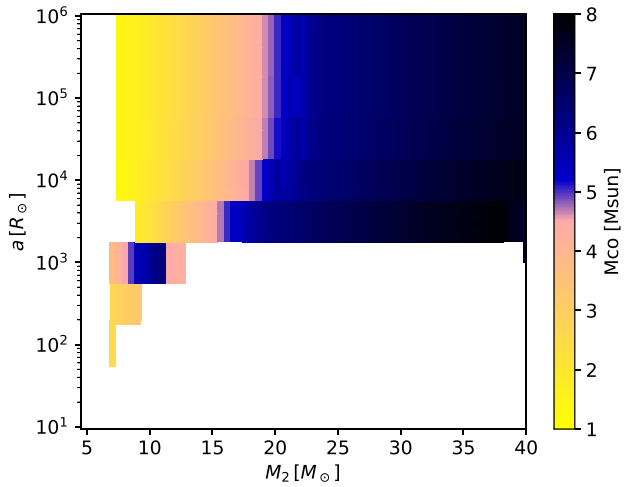

Figure B2. CO core mass of secondary star in the $q = 0.5$ case.

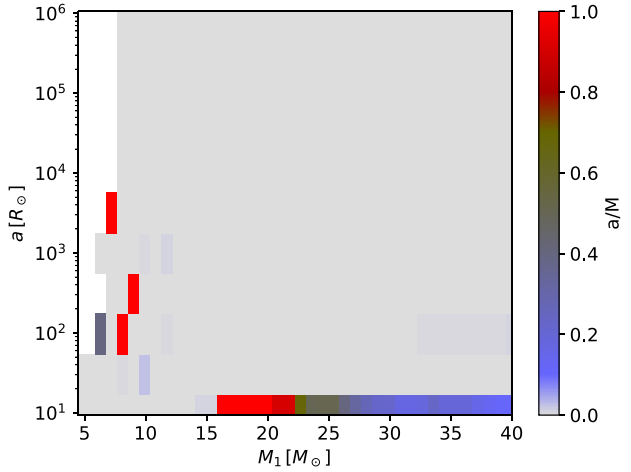

Figure B3. Angular momentum of primary star in the $q = 0.5$ case.

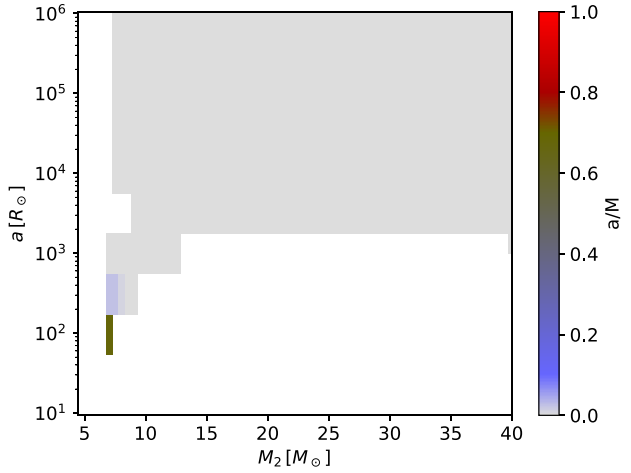

Figure B4. Angular momentum of secondary star in the $q = 0.5$ case.

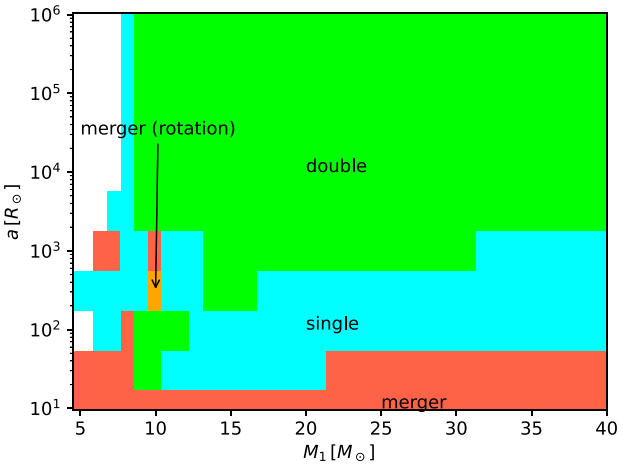

Figure B5. The binary progenitors of SNe in the $q = 0.9$ case.

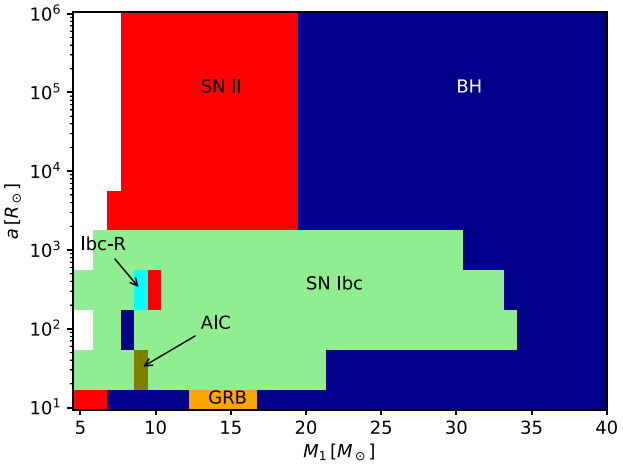

Figure B6. SN type of primary star in the $q = 0.9$ case.

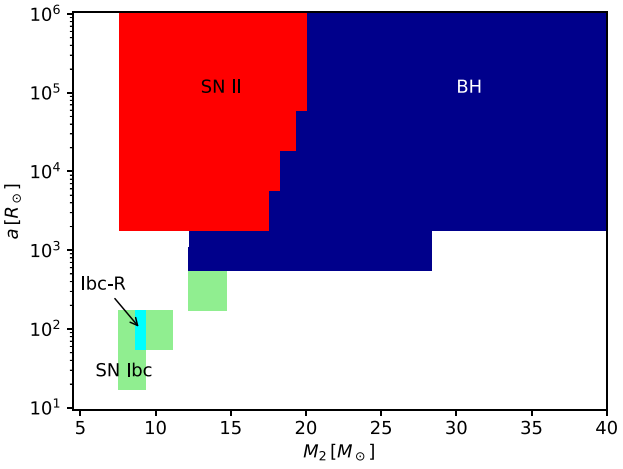

Figure B7. SN type of secondary star in the $q = 0.9$ case.

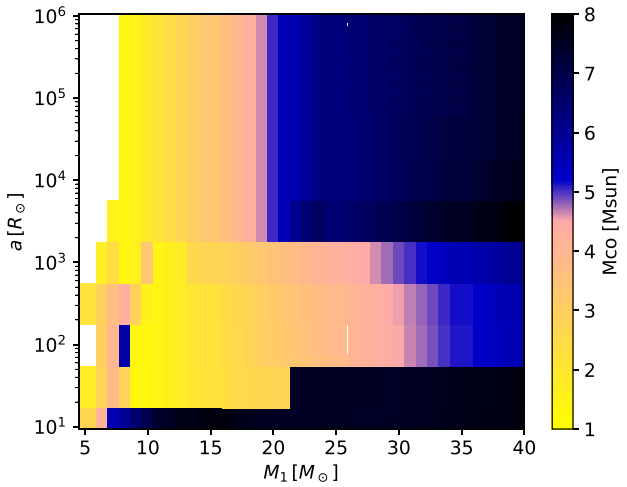

Figure B8. CO core mass of primary star in the $q = 0.9$ case.

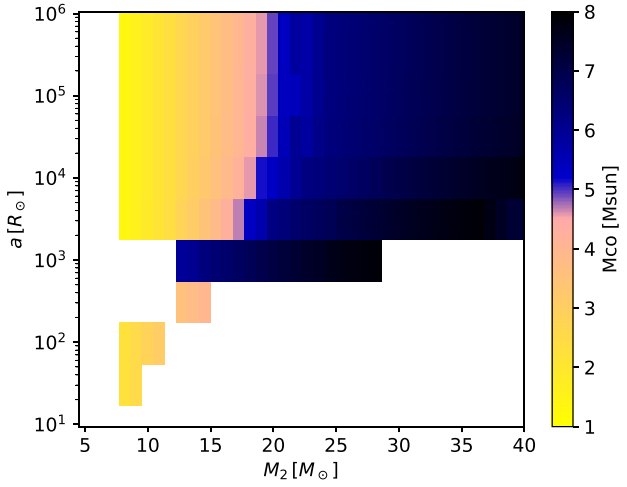

Figure B9. CO core mass of secondary star in the $q = 0.9$ case.

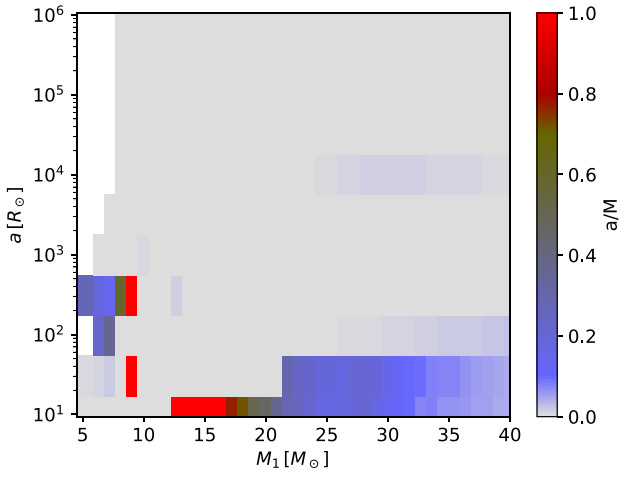

Figure B10. Angular momentum of primary star in the $q = 0.9$ case.

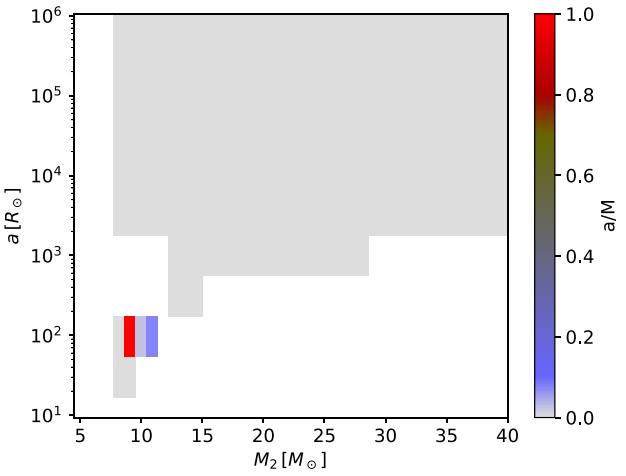

Figure B11. Angular momentum of secondary star in the $q = 0.9$ case.

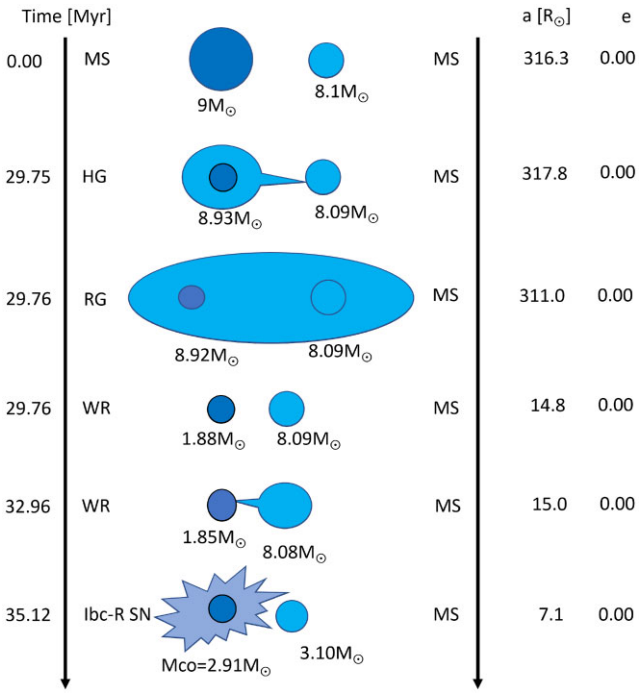

Figure B12. Example of the Ibc-R progenitor evolutionary path in the case of $q = 0.9$. See Fig. 10 for other examples with $q = 0.7$.

and they collapse via type II SNe, although their CO cores have large angular momentum.

The other difference is that the type Ibc SNe occurs by secondary stars whose masses are $11\,M_\odot \leq M_2 \leq 12.5\,M_\odot$ with $a = 10^3\,R_\odot$ (see Fig. A3). The SNe do not occur with the parameter range in $q = 0.7$ (see Fig. 3). BHs are formed from secondary stars whose masses are $9\,M_\odot \leq M_2 \leq 11\,M_\odot$ with $a = 10^3\,R_\odot$ and that is similar to case of $q = 0.7$. When secondary masses are $9\,M_\odot \leq M_2 \leq 11\,M_\odot$ with $a = 10^3\,R_\odot$, the secondary stars can become BHs due to the mass gain from the primary stars. However, when secondary masses are $11\,M_\odot \leq M_2 \leq 12.5\,M_\odot$ with $a = 10^3\,R_\odot$, they get such a lot of masses from the primary stars that they become a common envelope and loses hydrogen envelopes. After the common envelope phase,

the Wolf–Rayet stars lose a lot of masses due to the strong stellar wind mass-loss and they cannot collapse to BHs.

B2 q = 0.9 case

Fig. B5 shows the progenitor of the SN in the mass ratio $q = 0.9$. Figs B6 and B7 show the fate of the primary star and the secondary star, respectively, as a function of their ZAMS mass and binary separation. Figs B8 and B9 shows CO core mass as a function of their ZAMS mass and binary separation. Figs B10 and B11 show the angular momentum as a function of their ZAMS mass and binary separation.

The main differences of $q = 0.9$ case is another evolution path to Ibc-R. The point of $(M_1, a) = (9\,M_\odot, 10^{2.5}\,R_\odot)$ in Fig. B6 become Ibc-R. Fig. B12 shows the evolution path of this progenitor. The primary star loses the hydrogen envelope by the common envelope phase, but it can get enough mass and angular momentum by the mass transfer from the secondary star to occur a Ibc-R. The secondary star, whose initial mass is enough massive to become a SN, cannot become a SN due to a lot of mass loss.

APPENDIX C: THE FRACTIONS OF EACH SN TYPE FOR 12 MODELS

In order to calculate the fractions of each SN type for 12 models, we assume the binary fraction f_b as $f_b = 70$ per cent (e.g. Sana et al. 2012), and $f_b = 50$ per cent (e.g. Tian et al. 2018). According to Fig. 2, in the case of effectively single stars, relatively light stars ($8\,M_\odot < M < 20\,M_\odot$) tend to become type II SN, while more massive ones ($> 20\,M_\odot$) tend to become BH. If $f_b = 70$ per cent, the number of type II SN and the number of BH increase 8163 and 2959, respectively. If $f_b = 50$ per cent, the number of type II SN and the number of BH increase 19 049 and 6903, respectively. We added these values to our result, in order to calculate the fractions of each SN type. Tables C1 and C2 show the fractions of each SN type for 12 models with f_b =70 per cent, and f_b =50 per cent, respectively.

Table C1. The fractions of each SN type for 12 models with the binary fraction f_b =70 per cent.

Model	AIC	Ibc	II	Ibc-R	BH	long GRB
Sana_MT1_CE01	0.000467628	0.102274784	0.615594642	0.001131358	0.266774271	0.013757316
Sana_MT05_CE01	0.001097713	0.146470935	0.608640802	0.002539485	0.229831575	0.01141949
Sana_MT1_CE1	0.011630121	0.387514464	0.360665583	0.019012465	0.210499334	0.010678033
Sana_MT05_CE1	0.004391458	0.376396333	0.383175541	0.024545409	0.202741739	0.00874952
Sana_MT1_CE10	0.007020693	0.421914822	0.323432766	0.020212544	0.216551525	0.010867649
Sana_MT05_CE10	0.005627858	0.44880408	0.309743229	0.029827647	0.197414703	0.008582483
Abt_MT1_CE01	0.003723617	0.044735606	0.675227506	0.001183205	0.264168015	0.01096205
Abt_MT05_CE01	0.004687803	0.056306505	0.674127205	0.001057399	0.253352836	0.010468252
Abt_MT1_CE1	0.00780877	0.191621769	0.560782241	0.009598991	0.223010298	0.007177931
Abt_MT05_CE1	0.006059206	0.181438573	0.572461708	0.009755144	0.223586481	0.006698888
Abt_MT1_CE10	0.00974691	0.193383805	0.552446785	0.008795992	0.228640919	0.00698559
Abt_MT05_CE10	0.008735598	0.191768959	0.557515626	0.008603811	0.226786656	0.006589352

Table C2. The fractions of each SN type for 12 models with $f_b = 50$ per cent.

Model	AIC	Ibc	II	Ibc-R	BH	long GRB
Sana_MT1_CE01	0.00038214	0.083577821	0.637250068	0.000924533	0.266623111	0.011242326
Sana_MT05_CE01	0.000883136	0.117839348	0.633155827	0.002043076	0.236891361	0.009187251
Sana_MT1_CE1	0.009554638	0.318359587	0.42729931	0.015619547	0.22039446	0.008772458
Sana_MT05_CE1	0.003519854	0.301690333	0.452816553	0.019673711	0.215286607	0.007012942
Sana_MT1_CE10	0.005672326	0.340883484	0.402294831	0.016330601	0.226038308	0.00878045
Sana_MT05_CE10	0.004463663	0.355963175	0.397517087	0.023657414	0.211591575	0.006807086
Abt_MT1_CE01	0.002959848	0.035559674	0.687293398	0.000940513	0.264532994	0.008713572
Abt_MT05_CE01	0.003716485	0.044639738	0.686543808	0.000838305	0.255962444	0.008299219
Abt_MT1_CE1	0.006232819	0.152949022	0.59575134	0.00766174	0.231675785	0.005729294
Abt_MT05_CE1	0.004795522	0.14359847	0.606162457	0.00772065	0.232421106	0.005301794
Abt_MT1_CE10	0.00766752	0.152127629	0.591190264	0.006919469	0.236599822	0.005495296
Abt_MT05_CE10	0.006828952	0.149913166	0.596046861	0.006725929	0.235333942	0.005151149

This paper has been typeset from a TEX/LATEX file prepared by the author.